

Data-driven stochastic reduced-order modeling of parametrized dynamical systems

Andrew F. Ilersich, Kevin Course, Prasanth B. Nair

*University of Toronto Institute for Aerospace Studies,
4925 Dufferin Street, Toronto, ON M3H 5T6*

Abstract

Modeling complex dynamical systems under varying conditions is computationally intensive, often rendering high-fidelity simulations intractable. Although reduced-order models (ROMs) offer a promising solution, current methods often struggle with stochastic dynamics and fail to quantify prediction uncertainty, limiting their utility in robust decision-making contexts. To address these challenges, we introduce a data-driven framework for learning continuous-time stochastic ROMs that generalize across parameter spaces and forcing conditions. Our approach, based on amortized stochastic variational inference, leverages a reparametrization trick for Markov Gaussian processes to eliminate the need for computationally expensive forward solvers during training. This enables us to jointly learn a probabilistic autoencoder and stochastic differential equations governing the latent dynamics, at a computational cost that is independent of the dataset size and system stiffness. Additionally, our approach offers the flexibility of incorporating physics-informed priors if available. Numerical studies are presented for three challenging test problems, where we demonstrate excellent generalization to unseen parameter combinations and forcings, and significant efficiency gains compared to existing approaches.

1 Introduction

Numerical simulation of complex dynamical systems is computationally demanding, particularly in applications requiring multiple simulation runs under varying parameter settings and forcing conditions such as optimal design, parameter estimation, and control. Model order reduction is a powerful approach to address this challenge, wherein a reduced-order model (ROM) over a lower-dimensional latent space is constructed to serve as a computationally efficient surrogate/emulator of the full-order model (FOM). Arguably, the earliest work on this topic dates back to Fox and Miura in 1971 [1], who proposed projection schemes for accelerating structural design calculations. There is now a rich body of literature on the theoretical and computational aspects of projection-based ROMs for a broad class of parametrized operator problems [2].

A major limitation of projection-based ROM approaches is that they require direct access to the FOM. In many practical applications, the underlying FOM may be inaccessible, too complex to work with, or entirely unknown with the trajectory observations arising from experimental studies. This has motivated the development of data-driven ROM algorithms capable of learning directly from observed FOM or experimental trajectories, circumventing the need for explicit knowledge of the governing equations.

Most of the existing ROM approaches, whether projection-based or data-driven, proceed in two steps: first constructing forward and approximate inverse mappings between the full-order state and a low-dimensional latent state, then formulating equations governing the latent dynamics. The effectiveness of dimensionality reduction in this first step is fundamentally linked to the Kolmogorov n -width of the solution manifold, which quantifies the best possible approximation of the dynamics in a low-dimensional subspace [3]. For problems with rapidly decaying Kolmogorov n -width, linear dimensionality reduction techniques such as proper orthogonal decomposition (POD) have proven highly effective [4, 5, 2, 6, 7, 8]. However, many complex systems exhibit solution manifolds with slowly decaying n -width, motivating the use of nonlinear dimensionality reduction approaches [9, 10, 11, 12, 13, 14, 15, 16], basis adaptation algorithms [17], and

*andrew.ilersich@mail.utoronto.ca, kevin.course@mail.utoronto.ca, prasanth.nair@utoronto.ca

gradient-based reduction methods [18]. Projection-based methods leverage the FOM in the second step [19, 2, 12, 13], whereas data-driven approaches employ a non-intrusive approach involving the minimization of an appropriate loss function over training trajectories to estimate the ROM parameters [5, 10, 6, 7, 20, 21].

Even though the two-step approach has been applied successfully in many applications, it is worth noting that for certain datasets and latent mappings, the latent state trajectories learned in the first step can cross each other. In such scenarios, it is impossible to represent the dynamics with a system of differential equations [22]. Some studies approach ROM by simultaneously learning the state space mappings and the ROM dynamics, which avoids this issue [23, 24, 25].

Champion et al. [24] proposed a data-driven ROM method that simultaneously learns the state space mapping along with a sparse identification of nonlinear dynamics (SINDy) ROM. Similar to the approach presented in this work, the SINDy method also does not require a forward solver during training. However, this is achieved by assuming that the time-derivative of the state is available or can be computed using numerical differentiation. In the latter case, the accuracy of the ROM can deteriorate if the measurement noise variance is high. In contrast, the proposed approach requires only the state measurements to infer a ROM.

In the present work, we develop an amortized stochastic variational inference (SVI) scheme for learning ROMs across parameter spaces and forcing conditions using only FOM trajectory data. Our end-to-end methodology simultaneously infers a variational autoencoder for state space mapping and a system of continuous-time stochastic differential equations (SDEs) governing the latent dynamics. The present work advances data-driven ROM in the following ways: (1) by learning SDE-based ROMs, our approach can address challenging problems with stochastic dynamics (see, for example, [26, 27, 28]), (2) the end-to-end learning approach developed here circumvents the technical challenges associated with two-step methods described earlier, and (3) by adopting a stochastic modeling and inference framework, our approach enables quantification of prediction uncertainty, which is critical for downstream decision-making applications such as optimal design and control.

Although learning SDEs in a variational inference setting offers several theoretical advantages, its implementation poses significant computational challenges. Traditional approaches require integrating the latent SDE using a forward solver for each training trajectory to calculate the evidence lower bound and its gradients [29, 30, 31]. The need for a forward solver in the training loop, which is a well-known known bottleneck in training neural differential equations in general [32], can make the training cost prohibitive for high-dimensional states and large-scale datasets. Moreover, parameter updates during the inference process tends to increase the stiffness of the underlying differential equations, precipitating a blow-up in the cost per iteration.

We address these challenges by leveraging a reparametrization trick recently proposed by Course and Nair [33] that allows us to train the ROM *without* integrating it, which not only reduces the training cost, but decouples it from the SDE stiffness. Combined with an amortization strategy [34], our approach enables further reductions in training cost by defining variational distributions over short partitions of the time-domain. We present numerical studies on three test cases to demonstrate the efficacy of the proposed ROM approach in comparison to existing approaches. In the final test case, we consider ROM of a controlled fluid flow problem with 105,600 states, to demonstrate the scalability of our approach.

2 Methodology

2.1 Problem statement

Consider a parametrized spatio-temporal quantity of interest (QoI): $\tilde{u} : \Omega \times [0, T] \times \mathcal{F}_\mu \times \mathcal{F}_f \rightarrow \mathbb{R}$, either computed using a FOM or obtained through experimental measurements over the time interval $[0, T]$. Here, $\Omega \subset \mathbb{R}^m$ denotes the spatial domain, while $\mathcal{F}_\mu \subset \mathbb{R}^{N_\mu}$ and $\mathcal{F}_f \subseteq L^2(\Omega \times [0, T]; \mathbb{R})$ represent the parameter space and the space of forcing functions, respectively. Our training dataset comprises N_T noisy trajectories of the QoI under varying parameters and forcing functions, i.e., $\mathcal{D} := \{(\mu_i, \tilde{f}_i, \tilde{u}_i)\}_{i=1}^{N_T}$, where $\mu_i \in \mathcal{F}_\mu$, $\tilde{f}_i \in \mathcal{F}_f$, and $\tilde{u}_i \equiv \tilde{u}(x, t; \mu_i, \tilde{f}_i)$ with $x \in \Omega$, and $t \in [0, T]$.

In practice, we work with discrete representations of the QoI and forcing function involving D and N_f terms, respectively, that are obtained through spatial discretization on a mesh or by projecting onto

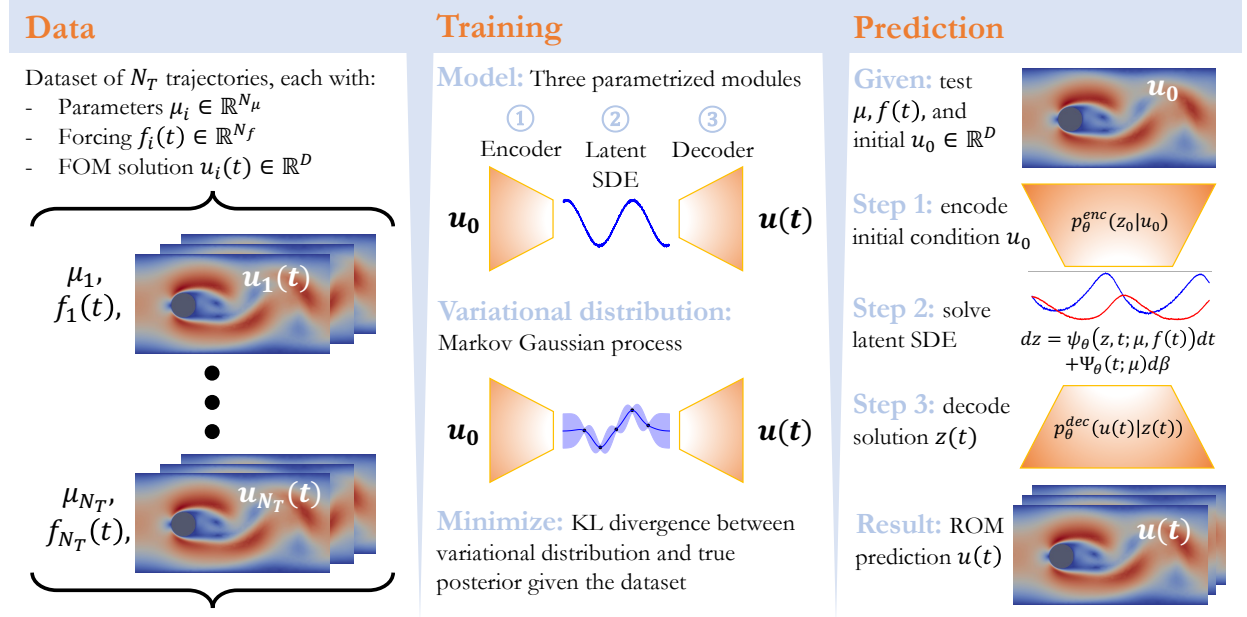


Figure 1: Graphical overview of the proposed stochastic ROM approach. The ROM, which we train by stochastic variational inference, consists of three modules: a probabilistic encoder, a latent SDE, and a probabilistic decoder. Making a prediction with the ROM starts with parameters μ , forcing $f(t)$, and initial condition u_0 . We encode the initial condition to obtain the corresponding latent z_0 . We then solve the latent SDE to obtain realizations of the trajectory $z(t)$. Decoding the sampled trajectories yields the stochastic ROM prediction of the FOM QoI, $u(t)$, that can be postprocessed for the mean prediction and statistical error bars.

appropriate sets of spatial basis functions. These discrete representations are sampled at time stamps $t_{i,j} \in [0, T]$, where $i = 1, 2, \dots, N_T$ indexes trajectories and $j = 1, 2, \dots, N_i$ indexes observations within each trajectory. We denote the spatially discretized forcing function and QoI as $f(t) \in \mathbb{R}^{N_f}$ and $u(t; \mu, f) \in \mathbb{R}^D$, respectively. For brevity, f_i and u_i will refer to these quantities in the i th trajectory.

The ROM we seek to learn involves a d -dimensional latent state vector z (with $d \ll D$), whose dynamics are governed by the following system of SDEs,

$$dz = \psi_\theta(z, t; \mu, f(t))dt + \Psi_\theta(t; \mu)d\beta, \quad z(0) \sim p_\theta^{\text{enc}}(z_0 | u_0(\mu)), \quad (1)$$

where $\psi_\theta : \mathbb{R}^d \times [0, T] \times \mathcal{F}_\mu \times \mathbb{R}^{N_f} \rightarrow \mathbb{R}^d$ and $\Psi_\theta : [0, T] \times \mathcal{F}_\mu \rightarrow \mathbb{R}^{d \times d}$ denote the drift function and dispersion matrix, respectively, and β denotes a d -dimensional Wiener process. The initial condition of the latent state is specified by the probabilistic encoder $p_\theta^{\text{enc}}(z_0 | u_0(\mu))$, where $z_0 \in \mathbb{R}^d$, and $u_0(\mu) \in \mathbb{R}^D$ denotes the initial condition of the full-order QoI. In addition, we introduce a probabilistic decoder $p_\theta^{\text{dec}}(u(t; \mu, f) | z(t; \mu, f))$ that maps the latent state to the full-order QoI, where $z(t; \mu, f) \in \mathbb{R}^d$ refers to the solution of (1) at time t for a given $\mu \in \mathcal{F}_\mu$ and $f \in L^2([0, T]; \mathbb{R}^{N_f})$.¹ We use the symbol θ to denote the learnable parameters of the encoder, decoder, drift and dispersion models.

A graphical overview of our stochastic ROM framework is presented in Figure 1. The framework consists of three parametrized components: a latent SDE model, a probabilistic encoder, and a probabilistic decoder. The drift and diffusion functions of the latent SDE can be parametrized using feedforward neural networks, yielding a ROM in the format of neural SDEs (NSDEs), while the probabilistic encoder and decoder can be parametrized using convolutional neural networks (CNNs). Our framework extends beyond these choices and can accommodate other neural network architectures, including graph neural networks, recurrent neural networks, and transformers. Moreover, our framework also allows for the incorporation of physics-informed

¹In practical settings, where the forcing is only specified/available at discrete time-stamps, f can be defined as a continuous-time interpolant of these samples.

parametrizations of the latent SDE; the drift function can be parametrized as $\psi_\theta = \psi^p + \psi_\theta^c$, where ψ^p is a known physics-based prior (for example, obtained by Galerkin projection [12]) and ψ_θ^c is a parametrized correction term. If the goal is to learn interpretable latent dynamics, the drift function can be parametrized using a basis function expansion combined with a sparsity-inducing prior [33].

To learn the posterior distributions of the latent state and model parameters, we develop an efficient amortized SVI scheme. We first specify the prior distributions and variational approximations for the latent state and model parameters. We then formulate an evidence lower bound (ELBO) that, when maximized, minimizes the Kullback-Leibler (KL) divergence between the approximate and true posteriors. We show how the ELBO can be reparametrized to eliminate the need for a forward solver during training. Finally, we develop an amortization strategy that decouples the computational cost and memory requirements of evaluating the ELBO from the dataset size. After training, the stochastic ROM can be used to make probabilistic predictions for new parameter settings and forcing conditions as illustrated in Figure 1.

2.2 Priors and variational approximations

In our ROM framework, the latent state z is a continuous-time stochastic process whose prior is defined by the solution of the nonlinear SDE in (1). Our approach defines the variational approximation of the latent state, $q_\phi(z | t; \mu, f)$, implicitly through the solution of the linear SDE

$$dz = (-A_\phi(t; \mu, f(t))z + b_\phi(t; \mu, f(t))) dt + \Psi_\theta(t; \mu) d\beta, \quad z(0) \sim \mathcal{N}(m_0(\mu), S_0(\mu)), \quad (2)$$

where $A_\phi(t; \mu, f(t)) \in \mathbb{R}^{d \times d}$, $b_\phi(t; \mu, f(t)) \in \mathbb{R}^d$, $m_0(\mu) \in \mathbb{R}^d$, and $S_0(\mu) \in \mathbb{R}^{d \times d}$. While this linear SDE representation of q_ϕ might seem limiting, it serves purely as a variational approximation during training – the actual ROM predictions employ the nonlinear SDE in (1).

For the model parameters θ , we may additionally specify a prior $p(\theta)$ and corresponding variational approximation $q_\phi(\theta)$. For instance, when seeking interpretable models, we can parametrize the drift function as a linear combination of basis functions and specify a sparsity-inducing prior on its coefficients [33]. Similarly, we can specify a log-normal prior to constrain the variance of the decoder $p_\theta^{\text{dec}}(u | z)$. The variational parameters ϕ encompass both the latent state and model parameter posterior approximations. We note that point estimates can also be learned for some or all components of θ in place of variational approximations; see Section 2.7 for details.

2.3 Evidence lower bound (ELBO)

The ELBO is a tractable lower bound on the evidence that serves as an objective function for estimating the variational parameters. Following the derivation in [30, 33], the ELBO for the ROM learning problem can be written as follows:

$$\begin{aligned} \mathcal{L}(\phi) = & \underbrace{\sum_{i=1}^{N_T} \sum_{j=1}^{N_i} \mathbb{E}_{z_{i,j}, \theta} [\log p_\theta^{\text{dec}}(u_i(t_{i,j}; \mu_i, f_i) | z_{i,j})]}_{\text{Log-likelihood term}} \\ & - \underbrace{\sum_{i=1}^{N_T} \frac{1}{2} \int_0^T \mathbb{E}_{z_i(t), \theta} \|r_{\theta, \phi}(z_i(t), t, \mu_i, f_i(t))\|_{C_\theta(t; \mu_i)}^2 dt}_{\text{Drift residual term}} - \underbrace{D_{\text{KL}}(q_\phi(\theta) \| p(\theta))}_{\text{Prior KL term}}, \end{aligned} \quad (3)$$

where $r_{\theta, \phi}(z_i(t), t, \mu_i, f_i(t)) = -A_\phi(t; \mu_i, f_i(t))z_i(t) + b_\phi(t; \mu_i, f_i(t)) - \psi_\theta(z_i(t), t; \mu_i, f_i(t))$,

with $z_{i,j} \sim q_\phi(z | t_{i,j}; \mu_i, f_i)$, $z_i(t) \sim q_\phi(z | t; \mu_i, f_i)$, and $\theta \sim q_\phi(\theta)$, where $r_{\theta, \phi}(z_i(t), t, \mu_i, f_i(t))$ denotes the drift residual corresponding to the i th trajectory in the training dataset, $D_{\text{KL}}(q_\phi(\theta) \| p(\theta))$ is the KL divergence between the variational posterior and the prior on θ , and $C_\theta(t; \mu_i) = (\Psi_\theta(t; \mu_i)\Psi_\theta^T(t; \mu_i))^{-1}$.

Evaluating the ELBO requires solving the variational SDE in (2) for each training trajectory to compute the expectations over $z_{i,j}$ in the log-likelihood term and over z_i in the drift residual term. This creates a computational bottleneck, particularly for large training datasets and high-dimensional latent states. The following reparametrization addresses this challenge.

2.4 Reparametrized ELBO

We leverage a reparametrization trick for SDE learning proposed by Course and Nair [33] that eliminates the need for a forward solver when computing the ELBO. We begin by noting that the solution of (2) is a Markov Gaussian process, i.e., $q_\phi(z \mid t; \mu, f) = \mathcal{N}(m_\phi(t; \mu, f), S_\phi(t; \mu, f))$. The dynamics of the mean $m_\phi(t; \mu, f) \in \mathbb{R}^d$ and covariance $S_\phi(t; \mu, f) \in \mathbb{R}^{d \times d}$ are governed by the ordinary differential equations: $\dot{m}_\phi = -A_\phi m_\phi + b_\phi$ and $\dot{S}_\phi = -A_\phi S_\phi - S_\phi A_\phi^T + \Psi_\theta \Psi_\theta^T$, with the initial conditions $m_\phi(0; \mu, f) = m_0(\mu)$ and $S_\phi(0; \mu, f) = S_0(\mu)$ [35]. The key insight from [33] is that by expressing A_ϕ and b_ϕ in terms of m_ϕ and S_ϕ , the ELBO can be reparametrized in terms of m_ϕ and S_ϕ .

The reparametrized ELBO retains the structure of (3), but introduces two crucial changes. First, the expectations in the ELBO are taken using samples drawn from $\mathcal{N}(m_\phi, S_\phi)$ which does not require a forward solver, i.e., $z_{i,j} \sim \mathcal{N}(m_\phi(t_{i,j}; \mu_i, f_i), S_\phi(t_{i,j}; \mu_i, f_i))$, and $z_i(t) \sim \mathcal{N}(m_\phi(t; \mu_i, f_i), S_\phi(t; \mu_i, f_i))$. Second, the original drift residual is replaced with the following reparametrized drift residual that depends only on m_ϕ and S_ϕ :

$$r_{\theta, \phi}(z_i(t), t, \mu_i, f_i) = B(m_\phi(t; \mu_i, f_i) - z_i(t)) + \dot{m}_\phi(t; \mu_i, f_i) - \psi_\theta(z_i(t), t; \mu_i, f_i), \quad (4)$$

where $B = \text{vec}^{-1} \left((S_\phi \oplus S_\phi)^{-1} \text{vec}(\Psi_\theta \Psi_\theta^T - \dot{S}_\phi) \right)$, \oplus denotes the Kronecker sum, $\text{vec} : \mathbb{R}^{d \times d} \rightarrow \mathbb{R}^{d^2}$ is an operator that maps a matrix to a vector by stacking columns, and $\text{vec}^{-1} : \mathbb{R}^{d^2} \rightarrow \mathbb{R}^{d \times d}$ denotes its inverse. The time-derivatives of the variational mean and covariance in the reparametrized drift residual are given by

$$\begin{aligned} \dot{m}_\phi(t; \mu, f) &= \frac{\partial m_\phi}{\partial t}(t; \mu, f) + \frac{\partial m_\phi}{\partial f}(t; \mu, f) \dot{f}(t), \\ \dot{S}_\phi(t; \mu, f) &= \frac{\partial S_\phi}{\partial t}(t; \mu, f) + \frac{\partial S_\phi}{\partial f}(t; \mu, f) \dot{f}(t). \end{aligned} \quad (5)$$

Despite the significant computational advantages of the reparametrized ELBO, two limitations remain. First, similar to (3), the reparametrized ELBO does not depend on the encoder $p_\theta^{\text{enc}}(z_0 \mid u_0(\mu))$, which is necessary for initializing the latent state when making ROM predictions. Second, the variational approximation for the latent state is defined over the entire time interval $[0, T]$ and space of forcings \mathbb{R}^{N_f} , potentially limiting its effectiveness for modeling complex dynamics over long time horizons. We address these limitations through an amortization strategy.

2.5 Amortized SVI with continuous-time encoding

We adopt an amortization strategy [34], where the variational distribution of the latent state is learned over partitions of $[0, T]$. Consider the i th trajectory where the time-stamps are given by $\{t_{i,1}, t_{i,2}, \dots, t_{i,N_i}\}$, where $t_{i,1} = 0$ and $t_{i,N_i} = T$. With window size M , we partition the time interval $[0, T]$ into N_i/M non-overlapping subintervals (if N_i is not divisible by M , we use a smaller partition size for the last subinterval) as follows:

$$\left\{ \left\{ t_{i,1}^{(1)}, \dots, t_{i,M}^{(1)} \right\}, \left\{ t_{i,1}^{(2)}, \dots, t_{i,M}^{(2)} \right\}, \dots, \left\{ t_{i,1}^{(N_i/M)}, \dots, t_{i,M}^{(N_i/M)} \right\} \right\}, \quad (6)$$

where we set $t_{i,M}^{(k)} = t_{i,1}^{(k+1)}$ for $k = 1, 2, \dots, N_i/M - 1$.

The variational distribution of the latent state can be subsequently amortized over the time partitions. More specifically, the variational distribution of the latent state over the k th time partition for the i th trajectory is written as $q_\phi(z \mid t; \mu_i, f_i, \mathcal{D}_{i,k}) = \mathcal{N}(m_\phi(t; \mu_i, f_i, \mathcal{D}_{i,k}), S_\phi(t; \mu_i, f_i, \mathcal{D}_{i,k}))$, where $t \in [t_{i,1}^{(k)}, t_{i,M}^{(k)}]$ and $\mathcal{D}_{i,k} := \{u_i(t_{i,j}^{(k)}; \mu_i, f_i)\}_{j=1}^M$ denotes the FOM QoI observations within the k th time partition for the i th trajectory. The amortized ELBO takes the form

$$\begin{aligned} \mathcal{L}(\phi) &= \sum_{i=1}^{N_T} \sum_{k=1}^{N_i/M} \left(\sum_{j=1}^M \mathbb{E}_{z_{i,j}^{(k)}, \theta} \left[\log p_\theta^{\text{dec}} \left(u_i(t_{i,j}^{(k)}; \mu_i, f_i) \mid z_{i,j}^{(k)} \right) \right] \right. \\ &\quad \left. - \frac{1}{2} \int_{t_{i,1}^{(k)}}^{t_{i,M}^{(k)}} \mathbb{E}_{z_i^{(k)}(t), \theta} \left[\left\| r_{\theta, \phi}(z_i^{(k)}(t), t, \mu_i, f_i(t)) \right\|_{C_\theta(t; \mu_i)}^2 \right] dt \right) - D_{\text{KL}}(q_\phi(\theta) \parallel p(\theta)), \end{aligned} \quad (7)$$

with $z_{i,j}^{(k)} \sim \mathcal{N}(m_\phi(t_{i,j}^{(k)}; \mu_i, f_i, \mathcal{D}_{i,k}), S_\phi(t_{i,j}^{(k)}; \mu_i, f_i, \mathcal{D}_{i,k}))$, $z_i^{(k)}(t) \sim \mathcal{N}(m_\phi(t; \mu_i, f_i, \mathcal{D}_{i,k}), S_\phi(t; \mu_i, f_i, \mathcal{D}_{i,k}))$, and $\theta \sim q_\phi(\theta)$.

To construct the latent variational distribution, we apply a two-step process within each partition. First, the QoI samples from the partition are passed as inputs to the encoder $p_\theta^{\text{enc}}(z | u)$. Then, we apply a deep-kernel interpolation scheme to these encoded values, yielding a continuous-time representation of $m_\phi(t)$ and $S_\phi(t)$.

We use a diagonal parametrization of S_ϕ to ensure parameter efficiency for large values of d , and denote the diagonal entries of S_ϕ by the d -dimensional vector s_ϕ . We next define a CNN that maps the QoI snapshot to the latent state mean and variance, i.e., $(m_\phi(t; \mu, f), \log(s_\phi(t; \mu, f))) = \mathcal{Y}(u(t; \mu, f))$. A log transformation is used to ensure that all entries of s_ϕ are strictly positive. It is worth noting here that, while making predictions, this CNN will serve as the encoder for the latent initial condition of our ROM in (1) given the QoI initial condition, i.e., $p_\theta^{\text{enc}}(z_0 | u_0(\mu)) = \mathcal{N}(m_0(\mu), S_0(\mu))$, where $S_0(\mu) = \text{diag}(s_0(\mu))$ and $(m_0(\mu), \log s_0(\mu)) = \mathcal{Y}(u_0(\mu))$. The CNN \mathcal{Y} takes the QoI snapshot $u_i(t_{i,j}^{(k)}; \mu_i, f_i)$ as input and its outputs are the mean and log-variance of the Gaussian distribution for $z_{i,j}^{(k)}$. This parametrization enables all the expectations in the log-likelihood term of the ELBO in (7) to be evaluated.

The continuous-time representation of the variational parameters m_ϕ and S_ϕ over the k th time partition for each trajectory must be differentiable to permit evaluation of the reparametrized drift residual in (4). To proceed further, we first evaluate the CNN \mathcal{Y} over all snapshots of the QoI in the k th time partition for the i th trajectory. This leads to the matrix of feature vectors $H_m = [m_{i,1}^{(k)}, m_{i,2}^{(k)}, \dots, m_{i,M}^{(k)}]^T \in \mathbb{R}^{M \times d}$ and $H_s = [\log s_{i,1}^{(k)}, \log s_{i,2}^{(k)}, \dots, \log s_{i,M}^{(k)}]^T \in \mathbb{R}^{M \times d}$, where $(m_{i,j}^{(k)}, \log s_{i,j}^{(k)}) = \mathcal{Y}(u_i(t_{i,j}^{(k)}; \mu_i, f_i))$, $j = 1, 2, \dots, M$. We then apply the deep kernel interpolation scheme from [34] to the feature vectors in H_m and H_s to arrive the following continuous-time representations of m_ϕ and S_ϕ :

$$\begin{aligned} m_\phi(t; \mu_i, f_i) &= K_M(t) (K_{MM} + \sigma^2 I)^{-1} H_m, \\ \log s_\phi(t; \mu_i, f_i) &= K_M(t) (K_{MM} + \sigma^2 I)^{-1} H_s, \end{aligned} \quad (8)$$

where $t \in [t_{i,1}^{(k)}, t_{i,M}^{(k)}]$, $K_M(t)$ is a row vector of length M whose entries are given by $\kappa(t, t_{i,j}^{(k)}), j = 1, 2, \dots, M$, K_{MM} is an $M \times M$ matrix whose entries are $\kappa(t_{i,j}^{(k)}, t_{i,j'}^{(k)}), j = 1, 2, \dots, M, j' = 1, 2, \dots, M$, I is the identity matrix of size M , and $\kappa : \mathbb{R} \times \mathbb{R} \rightarrow \mathbb{R}$ denotes a deep kernel that is defined as $\kappa(t_1, t_2) = \sigma_f \exp(-\|\varphi(t_1) - \varphi(t_2)\|^2/(2\ell^2))$, where $\varphi : \mathbb{R} \rightarrow \mathbb{R}$ is a deep feedforward neural network. The parameter σ_f controls the amplitude of the kernel and ℓ determines the length scale. The parameters $\sigma, \sigma_f, \ell \in \mathbb{R}^+$ are estimated along with other model parameters during training.

Note that following (8), the effect of forcing on m_ϕ and S_ϕ is contained in the H_m and H_s terms respectively, which are constant. The only time-dependency is via the kernel vector $K_M(t)$, which makes the chain rule expansion in (5) unnecessary.

2.6 Gradient estimation

To estimate the gradient of the ELBO with respect to variational parameters ϕ , we use the standard reparametrization trick [36]. We express the reparametrized latent state as $z(t; \mu, f) = \mathcal{T}(t, \gamma, \phi) = m_\phi(t; \mu, f) + (S_\phi(t; \mu, f))^{1/2} \gamma$, where $\gamma \sim \mathcal{N}(0, I)$. Similarly, we express the reparametrized model parameters as $\theta = \mathcal{Q}(\xi, \phi)$, where $\xi \sim \mathcal{N}(0, I)$. The drift residual integral is approximated using a Monte Carlo scheme with time samples drawn from $\mathcal{U}[t_{i,1}^{(k)}, t_{i,M}^{(k)}]$. Taking R samples of γ , L time samples, and one sample of ξ , we obtain the following unbiased estimate of the ELBO gradient over the k th partition of the i th trajectory.

$$\begin{aligned} \nabla_\phi \mathcal{L}(\phi) &\approx \frac{1}{R} \sum_{r=1}^R \left(\sum_{j=1}^M \nabla_\phi \log p_\theta^{\text{dec}}(u_i(t_{i,j}^{(k)}; \mu_i, f_i) | z_{i,j,r}^{(k)}) \right. \\ &\quad \left. - \frac{t_{i,M}^{(k)} - t_{i,1}^{(k)}}{2L} \sum_{\ell=1}^L \nabla_\phi \|r_{\theta, \phi}(z_{\ell,r}, \tau_\ell, \mu_i, f_i(\tau_\ell))\|_{C_\theta(\tau_\ell; \mu_i)}^2 \right) - \nabla_\phi D_{\text{KL}}(q_\phi(\theta) \| p(\theta)), \end{aligned} \quad (9)$$

where $z_{i,j,r}^{(k)} = \mathcal{T}(t_{i,j}^{(k)}, \gamma_r, \phi)$, $z_{\ell,r} = \mathcal{T}(\tau_\ell, \gamma_r, \phi)$, the indices i and k are sampled uniformly from $\{1, 2, \dots, N_T\}$ and $\{1, 2, \dots, N_i/M\}$ respectively, $\theta = \mathcal{Q}(\xi, \phi)$ where ξ is a single sample drawn from $\mathcal{N}(0, I)$, $\gamma_1, \gamma_2, \dots, \gamma_R \sim \mathcal{N}(0, I)$, and $\tau_1, \tau_2, \dots, \tau_L \sim \mathcal{U}[t_{i,1}^{(k)}, t_{i,M}^{(k)}]$.

The key advantage of our reparametrization trick and amortized representation is that the computational complexity and memory requirements of our gradient estimator are independent of: (i) training dataset size (number of trajectories), (ii) time series length (number of samples per trajectory), and (iii) stiffness of either the underlying dynamics or the approximate SDE. More specifically, the computational complexity scales linearly with the sampling parameters R , M , and L . Furthermore, our approach enables massively parallel computation since each gradient term can be evaluated independently. This contrasts sharply with the original ELBO in (3), which depends on a strictly sequential SDE forward solver.

2.7 Point estimates of model parameters

For the case when a point estimate is sought for the parameter vector θ rather than a distribution $q_\phi(\theta)$, the amortized ELBO in (7) simplifies to

$$\begin{aligned} \mathcal{L}(\theta, \phi) &= \sum_{i=1}^{N_T} \sum_{k=1}^{N_i/M} \left(\sum_{j=1}^M \mathbb{E}_{z_{i,j}^{(k)}} \left[\log p_\theta^{\text{dec}} \left(u_i(t_{i,j}^{(k)}; \mu_i, f_i) \mid z_{i,j}^{(k)} \right) \right] \right. \\ &\quad \left. - \frac{1}{2} \int_{t_{i,1}^{(k)}}^{t_{i,M}^{(k)}} \mathbb{E}_{z_i^{(k)}(t)} \left\| r_{\theta, \phi}(z_i^{(k)}(t), t, \mu_i, f_i(t)) \right\|_{C_\theta(t; \mu_i)}^2 dt \right), \end{aligned} \quad (10)$$

with $z_{i,j}^{(k)} \sim \mathcal{N}(m_\phi(t_{i,j}^{(k)}; \mu_i, f_i, \mathcal{D}_{i,k}), S_\phi(t_{i,j}^{(k)}; \mu_i, f_i, \mathcal{D}_{i,k}))$ and $z_i^{(k)}(t) \sim \mathcal{N}(m_\phi(t; \mu_i, f_i, \mathcal{D}_{i,k}), S_\phi(t; \mu_i, f_i, \mathcal{D}_{i,k}))$. Note that the term $D_{KL}(q_\phi(\theta) \parallel p(\theta))$ is no longer present in the ELBO and we no longer take expectations over θ in the log-likelihood and drift residual terms. The unbiased estimate of the ELBO gradient over the k th partition of the i th trajectory then takes the following form (analogous to (9)):

$$\begin{aligned} \nabla_{\theta, \phi} \mathcal{L}(\theta, \phi) &\approx \frac{1}{R} \sum_{r=1}^R \left(\sum_{j=1}^M \nabla_{\theta, \phi} \log p_\theta^{\text{dec}} \left(u_i(t_{i,j}^{(k)}; \mu_i, f_i) \mid \mathcal{T}(t_{i,j}^{(k)}, \gamma_r, \phi) \right) \right. \\ &\quad \left. - \frac{t_{i,M}^{(k)} - t_{i,1}^{(k)}}{2L} \sum_{\ell=1}^L \nabla_{\theta, \phi} \left\| r_{\theta, \phi}(\mathcal{T}(\tau_\ell, \gamma_r, \phi), \tau_\ell, \mu_i, f_i(\tau_\ell)) \right\|_{C_\theta(\tau_\ell; \mu_i)}^2 \right), \end{aligned} \quad (11)$$

where the indices i and k are sampled uniformly from $\{1, 2, \dots, N_T\}$ and $\{1, 2, \dots, N_i/M\}$, respectively, $\gamma_1, \gamma_2, \dots, \gamma_R \sim \mathcal{N}(0, I)$, and $\tau_1, \tau_2, \dots, \tau_L \sim \mathcal{U}[t_{i,1}^{(k)}, t_{i,M}^{(k)}]$. We note that since θ is no longer a random variable, the reparameterization in terms of $\mathcal{Q}(\xi, \phi)$ is no longer necessary. Similar to (9), we express the reparametrized latent state as $z(t; \mu, f) = \mathcal{T}(t; \gamma, \phi) = m_\phi(t; \mu, f) + (S_\phi(t; \mu, f))^{1/2} \gamma$, where $\gamma \sim \mathcal{N}(0, I)$.

We now consider the case when point estimates are only sought for a subset of the model parameters in θ . Let $\widehat{\theta}$ denote the subset of parameters for which point estimates are sought while $\widetilde{\theta}$ denotes the set of model parameters for which a prior and variational approximation is specified (i.e., θ is decomposed into $(\widetilde{\theta}, \widehat{\theta})$). In this case, training the model yields a posterior distribution over $\widetilde{\theta}$, parametrized by ϕ , and a point estimate of $\widehat{\theta}$. In this setting, the ELBO takes the form

$$\begin{aligned} \mathcal{L}(\widehat{\theta}, \phi) &= \sum_{i=1}^{N_T} \sum_{k=1}^{N_i/M} \left(\sum_{j=1}^M \mathbb{E}_{z_{i,j}^{(k)}, \widetilde{\theta}} \left[\log p_\theta^{\text{dec}} \left(u_i(t_{i,j}^{(k)}; \mu_i, f_i) \mid z_{i,j}^{(k)} \right) \right] \right. \\ &\quad \left. - \frac{1}{2} \int_{t_{i,1}^{(k)}}^{t_{i,M}^{(k)}} \mathbb{E}_{z_i^{(k)}(t), \widetilde{\theta}} \left\| r_{\theta, \phi}(z_i^{(k)}(t), t, \mu_i, f_i(t)) \right\|_{C_\theta(t; \mu_i)}^2 dt \right) - D_{KL} \left(q_\phi(\widetilde{\theta}) \parallel p(\widetilde{\theta}) \right), \end{aligned} \quad (12)$$

with $z_{i,j}^{(k)} \sim \mathcal{N}(m_\phi(t_{i,j}^{(k)}; \mu_i, f_i, \mathcal{D}_{i,k}), S_\phi(t_{i,j}^{(k)}; \mu_i, f_i, \mathcal{D}_{i,k}))$ and $z_i^{(k)}(t) \sim \mathcal{N}(m_\phi(t; \mu_i, f_i, \mathcal{D}_{i,k}), S_\phi(t; \mu_i, f_i, \mathcal{D}_{i,k}))$. Note that the expectations in the log-likelihood and drift residual terms are now over $\widetilde{\theta}$, and the KL term is defined between the prior and variational approximation of $\widetilde{\theta}$.

To obtain an unbiased estimator for the gradients of the ELBO with respect to the variational parameters ϕ , and model parameters θ , we reparametrize θ as $\tilde{\theta} = Q(\xi, \phi)$ with $\xi \sim \mathcal{N}(0, I)$ and express the reparametrized latent state as $z(t; \mu, f) = \mathcal{T}(t, \gamma, \phi) = m_\phi(t; \mu, f) + (S_\phi(t; \mu, f))^{1/2}\gamma$ with $\gamma \sim \mathcal{N}(0, I)$. This yields

$$\begin{aligned} \nabla_{\hat{\theta}, \phi} \mathcal{L}(\hat{\theta}, \phi) &\approx \frac{1}{R} \sum_{r=1}^R \left(\sum_{j=1}^M \nabla_{\hat{\theta}, \phi} \log p_\theta^{\text{dec}}(u_i(t_{i,j}^{(k)}; \mu_i, f_i) \mid \mathcal{T}(t_{i,j}^{(k)}, \gamma_r, \phi)) \right. \\ &\quad - \frac{t_{i,M}^{(k)} - t_{i,1}^{(k)}}{2L} \sum_{\ell=1}^L \nabla_{\hat{\theta}, \phi} \|r_{\theta, \phi}(\mathcal{T}(\tau_\ell, \gamma_r, \phi), \tau_\ell, \mu_i, f_i(\tau_\ell))\|_{C_\theta(\tau_\ell; \mu_i)}^2 \Big) \\ &\quad - \nabla_\phi D_{\text{KL}}(q_\phi(\tilde{\theta}) \parallel p(\tilde{\theta})), \end{aligned} \quad (13)$$

where the indices i and k are sampled uniformly from $\{1, 2, \dots, N_T\}$ and $\{1, 2, \dots, N_i/M\}$, respectively, $\tilde{\theta} = Q(\xi, \phi)$ where ξ is a single sample drawn from $\mathcal{N}(0, I)$, $\gamma_1, \gamma_2, \dots, \gamma_R \sim \mathcal{N}(0, I)$, and $\tau_1, \tau_2, \dots, \tau_L \sim \mathcal{U}[t_{i,1}^{(k)}, t_{i,M}^{(k)}]$.

2.8 Probabilistic ROM predictions

To generate predictions with the trained ROM, we require an initial condition for the full-order QoI u_0 , system parameters μ , forcing function f , and a simulation time T . The prediction process involves the following steps:

1. Sample latent initial condition from encoder, $z(0) \sim p_\theta^{\text{enc}}(z_0 \mid u_0)$,
2. Evolve latent state by integrating (1), $z(T) \sim \int_0^T \psi_\theta(z, t; \mu, f(t)) dt + \int_0^T \Psi_\theta(t; \mu) d\beta$,
3. Generate QoI prediction by sampling from decoder, $u(T) \sim p_\theta^{\text{dec}}(u(T) \mid z(T))$.

This procedure forms the basis for our model evaluation in the numerical studies that follow.

3 Results

To comprehensively evaluate the efficacy and versatility of our proposed framework for learning stochastic ROMs, we conduct numerical studies on three challenging test problems. These range from learning sparse, interpretable dynamics in unforced systems, to handling complex parametrized and forced dynamics, and finally, to assessing scalability on a high-dimensional controlled fluid flow problem. The first test case is a non-parametrized, unforced reaction-diffusion system [24] that enables an evaluation of our approach's ability to infer sparse latent dynamics without requiring time-derivative observations. The second test case is a forced, parametrized one-dimensional Burgers' equation problem that introduces the challenge of learning ROMs that generalize across parameter spaces and forcing conditions, a scenario commonly encountered in many engineering applications. Finally, we study a controlled fluid flow problem [37] to demonstrate the scalability and practical applicability of our method to large-scale systems. In each study, ROMs are trained using a set of sample trajectories and their performance is rigorously assessed on a separate, unseen test set using the error metric: $\varepsilon(t) = \|u(t) - \bar{u}(t)\|/\|u(t)\|$, where $\bar{u}(t)$ is the mean ROM prediction and $u(t)$ denotes the true QoI.

We benchmark our approach against four established data-driven ROM techniques, spanning both neural differential equation models and sparse, interpretable model discovery frameworks. We consider two variants of latent SINDy, a framework for inferring sparse interpretable models [38, 39]. We implement these using the PySINDy library [40, 41]: (i) POD-SINDy, employing POD for dimensionality reduction, and (ii) AE-SINDy, utilizing a non-linear autoencoder. In addition, we also benchmark against parametrized neural ordinary differential equations (PNODEs) following [23] (implemented with the `torchdiffeq` library [42]), and an extension thereof into parametrized neural stochastic differential equations (PNSDEs) (implemented with the `torchsde` library [31]). Following Chen et al [42] and Rubanova et al. [43], we use an evidence lower bound as our loss; we detail the PNODE/PNSDE formulations in Section A. Note that the training of

Table 1: Reaction-diffusion: model comparison over mean error ε_μ , standard deviation of error ε_σ , and training time T_{tr} in hours. PA: present approach. AE-SINDy¹ is trained in a two-step manner using PysINDy. AE-SINDy² is trained in an end-to-end manner using the architecture and implementation from Champion et al.

Metric	Noiseless dataset				Noisy dataset			
	PA	POD-SINDy	AE-SINDy ¹	AE-SINDy ²	PA	POD-SINDy	AE-SINDy ¹	AE-SINDy ²
ε_μ	0.036	0.140	1.141	0.126	0.052	0.142	1.212	0.130
ε_σ	0.015	0.003	0.652	0.006	0.018	0.003	0.620	0.008
T_{tr}	3.698	0.009	0.629	1.699	3.630	0.014	0.613	1.603

PNODEs and PNSDEs relies on a forward solver, a bottleneck our approach aims to eliminate. Furthermore, PNODE/PNSDE architectures do not directly accommodate time-varying forcing functions; thus, for forced problems, we adopt the common practice of parametrizing the forcing via its characteristic parameters or POD coefficients. The PNODE and PNSDE baselines are trained using full-trajectory batches, a common practice for these methods. All models were trained for a comparable number of epochs to facilitate a fair comparison; for additional details see Section C.

Example 1: Reaction-diffusion system

We first consider a reaction-diffusion system previously studied by Champion et al. [24]. Details of the problem setup are given in Section C.1. The spatial domain is discretized using a grid with $D = 100 \times 100$ equispaced points, and the time domain is discretized using 9999 steps. We consider a single trajectory with fixed parameters and no forcing. The time interval is partitioned as follows: the interval $[0, 400]$ constitutes the training set, the next interval $(400, 450]$ is the validation set, and the final $(450, 500]$ is the test set. We set up the training data in a manner identical to Champion et al., except that whereas they corrupt the data (both v and its time derivative v_t , independently) using zero-mean Gaussian noise with standard deviation 10^{-6} , we consider two cases: a noiseless case, and a noisy case with standard deviation 10^{-2} .

Following Champion et al., we consider a two-dimensional latent state and parametrize the drift function ψ_θ as a third-order polynomial. The results obtained using different methods are summarized in Table 1. The table highlights the importance of the training strategy for latent SINDy models. Specifically, AE-SINDy¹, trained in a two-step manner, performs poorly; its autoencoder, optimized independently of the SINDy dynamics model, likely yields latent trajectories that are difficult for SINDy to represent accurately. In contrast, POD-SINDy, despite using a simpler linear encoder, achieves better results than AE-SINDy¹, possibly due to the inherent smoothness and regularity often associated with POD modes. The end-to-end training of AE-SINDy² demonstrates a significant improvement over both, underscoring the benefit of jointly optimizing the encoder and the latent dynamics.

Our approach (PA) provides better accuracy compared to all SINDy-based methods on both datasets. Notably, this higher accuracy is achieved using only state measurements, whereas all SINDy variants require time-derivative information. The test predictions of our stochastic ROM are shown in Figure 2 for both noiseless and noisy data. It can be seen that the stochastic ROM is able to capture the dynamics well, even in the presence of noise. The error growth over time is approximately linear, which can be attributed to the ROM drifting out of phase with the true trajectory.

Example 2: Forced, parametrized Burgers' equation

We next consider the viscous one-dimensional Burgers' equation over $x \in [0, 1]$ and $t \in [0, 3]$. This problem is parametrized by viscosity $\nu \in [0.05, 0.1]$ and the time-dependent forcing is given as $f(t) = \alpha_1 \cos(2\pi\omega t)$, where $\omega \in [0.8, 1]$. The initial condition is $v(x, 0) = \alpha_1 \exp(-x^2/\alpha_2)$, where $\alpha_1 = 5$ and $\alpha_2 = 0.001$. The forcing is applied to the left boundary, i.e., $v(0, t) = f(t)$, and the right boundary has a zero Dirichlet condition. We discretize the governing equations using a finite-difference scheme on a spatial mesh with

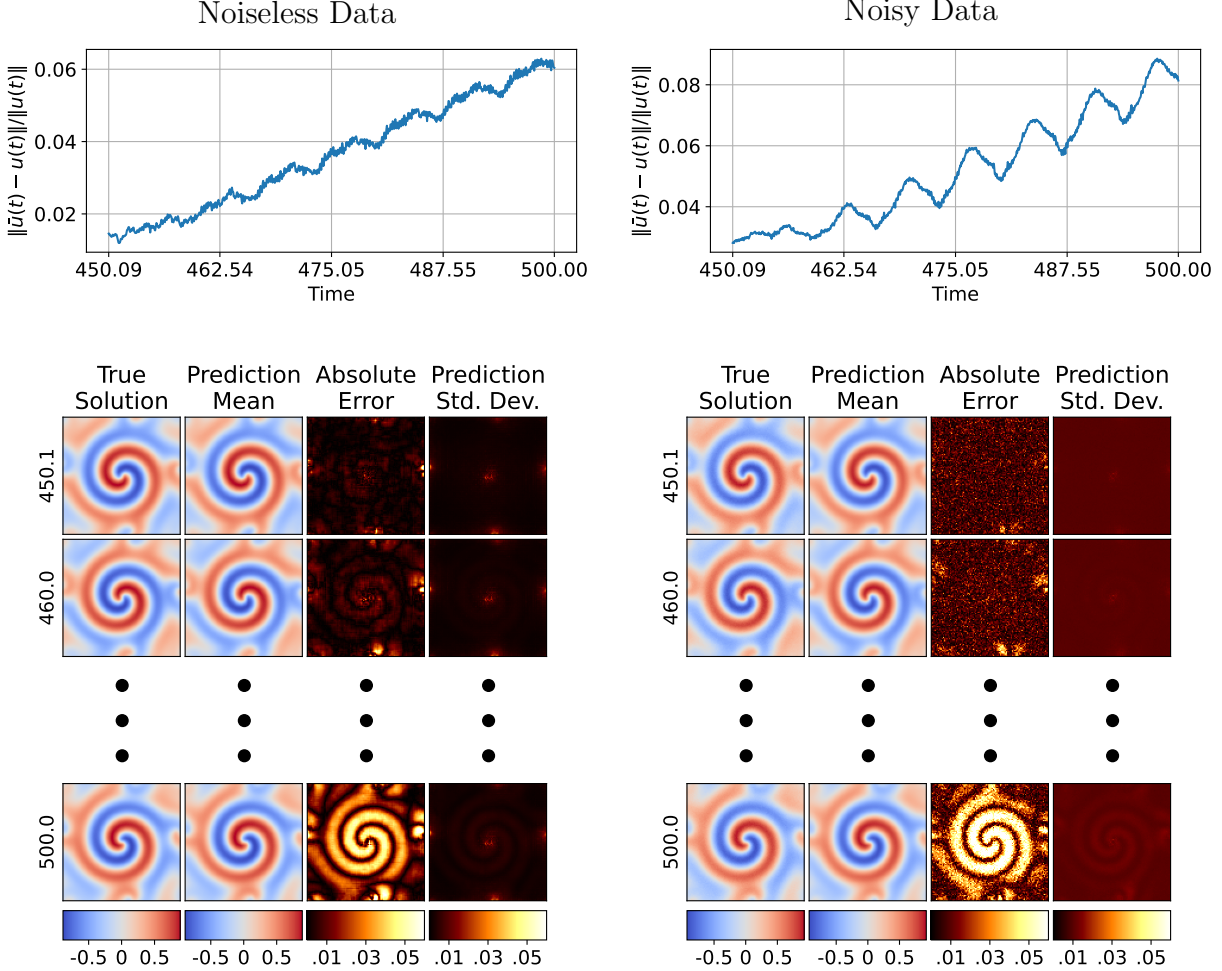


Figure 2: Reaction-diffusion: error evolution and predictions over time. The top row illustrates prediction error on the test interval for noiseless (left) and noisy (right) data. The bottom half shows the true solution, prediction mean, absolute error, and prediction standard deviation. See movies S1-S2.

$D = 500$ equispaced points and use a time-marching scheme with $\Delta t = 0.001$, resulting in 1001 time samples in each FOM trajectory.

We generate our dataset by running the FOM for different realizations of ν and ω . The training set contains 100 trajectories, the validation set contains 10, and the test set contains 10. Applying the principle for estimating intrinsic manifold dimensionality discussed by Lee and Carlberg [12], we observe that any state snapshot in our problem is determined by viscosity ν , forcing frequency ω , and time t . This implies a manifold dimension of at least 3, which we use as a lower bound to explore latent dimensions $d \in \{3, 4, 5\}$; see Section C.2 for additional details.

The results are summarized in Table 2. For this more complex problem with variations in parameters and forcing, the SINDy-based approaches (POD-SINDy and AE-SINDy) struggle to achieve competitive accuracy compared to the neural differential equation models, with AE-SINDy showing some improvement for $d = 4$. We observe considerable variation in PNODE/PNSDE prediction accuracy across different latent dimensions due to difficulties in converging to a model that generalizes well. In contrast, our proposed approach (PA) consistently delivers good accuracy, particularly for $d = 4$ and $d = 5$, while maintaining significantly shorter training times than PNODE/PNSDE. For instance, with $d = 4$, PA achieves a mean error of 0.065 with a training time of 3.281 hours, outperforming PNODE ($\varepsilon_\mu = 0.707$, $T_{\text{tr}} = 6.035$) and PNSDE ($\varepsilon_\mu = 0.718$,

Table 2: Burgers' equation: model comparison for varying ROM dim. d over mean error ε_μ , standard deviation of error ε_σ , and training time T_{tr} in hours. PA: present approach.

d	Metric	POD-SINDy				
		PA	AE-SINDy	PNODE	PNSDE	
3	ε_μ	0.081	0.903	0.961	0.075	0.086
	ε_σ	0.086	0.084	0.307	0.015	0.26
	T_{tr}	3.352	0.001	0.553	5.982	4.358
4	ε_μ	0.065	0.719	0.192	0.707	0.718
	ε_σ	0.028	0.092	0.111	0.004	0.009
	T_{tr}	3.281	0.001	0.552	6.035	4.407
5	ε_μ	0.067	0.569	0.276	0.162	0.175
	ε_σ	0.032	0.070	0.425	0.078	0.077
	T_{tr}	3.271	0.004	0.553	4.877	4.559

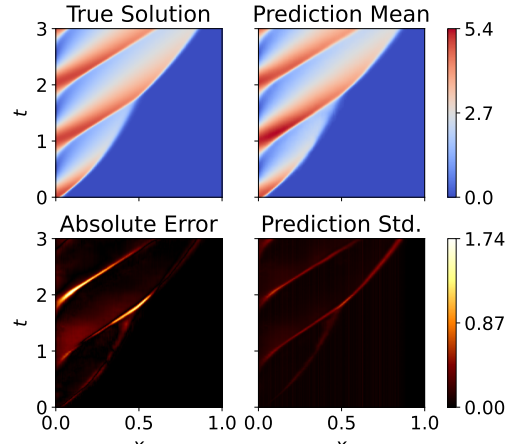


Figure 3: Burgers' equation: solution, error, & prediction statistics for a test trajectory. See movie S3.

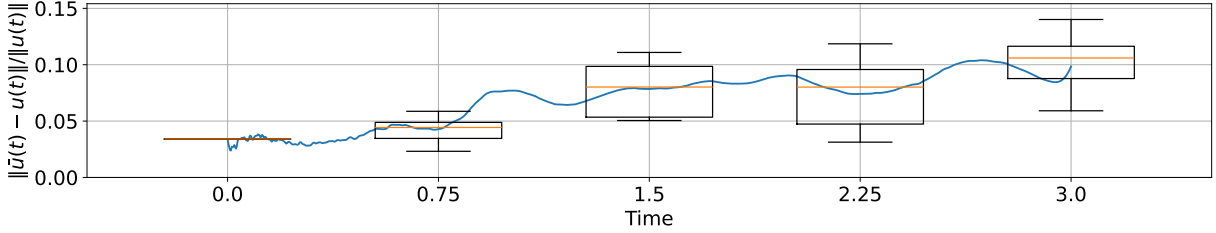


Figure 4: Burgers' equation: error distribution on test set over time for $d = 5$.

$T_{\text{tr}} = 4.407$) in both metrics. Figures 3 and 4 show visualizations of our stochastic ROM predictions. The error distribution plot shows that as shock boundaries form, local error increases sharply. Notably, the uncertainty in the stochastic ROM prediction is strongly correlated with these high-error regions, increasing along the shock boundaries.

Example 3: Fluid flow with control input

To demonstrate the scalability of our approach, we now consider two-dimensional fluid flow around a cylinder at $Re = 100$ with time-dependent forcing, a test case adapted from the work by Rabault et al. [37] on flow control of the Von Kármán vortex street using deep reinforcement learning. The forcing takes the form of jets on the top and bottom of the cylinder, whose flow rates Q_1 , Q_2 are controlled. No net mass is injected into or removed from the system by the jets, so $f(t) = Q_1 = -Q_2$. We model the flow rate as a zero-mean Gaussian process with covariance function $k(t_1, t_2) = \alpha \exp(-(t_1 - t_2)^2/(2\ell^2))$, where $\ell = T_v$ and $\alpha = 10^{-5}$.

The FOM in this case is a fluid flow simulation on an unstructured mesh [37]. The velocity and pressure fields on the mesh are resampled onto a 440×80 uniform spatial grid, leading to a $D = 105,600$ -dimensional state. We generate 120 training, 10 validation, and 10 test trajectories for different realizations of the flow rate over a time-interval spanning 2-times the vortex shedding period T_v . We vary the latent state dimension $d \in \{7, 8, 9\}$ for this test case; additional details can be found in Section C.3.

The results are summarized in Table 3. In this high-dimensional fluid flow problem, our approach consistently achieves the lowest mean prediction errors across all tested latent dimensions ($d = 7, 8, 9$) compared to the baselines. For instance, with $d = 9$, PA yields a mean error ε_μ of 0.036, outperforming PNODE (0.076), PNSDE (0.091), AE-SINDy (0.073), and POD-SINDy (0.095). The training time of our approach ($T_{\text{tr}} \approx 3.2$ hours) is substantially shorter than that of PNODE (19 – 26 hours) and PNSDE (≈ 19

Table 3: Fluid flow with control: model comparison for varying ROM dim. d over mean error ε_μ , standard deviation of error ε_σ , and training time T_{tr} in hours. PA: present approach.

d	Metric	POD-		AE-		
		PA	SINDy	SINDy	PNODE	PNSDE
7	ε_μ	0.043	0.088	0.078	0.100	0.095
	ε_σ	0.030	0.026	0.046	0.030	0.025
	T_{tr}	3.223	0.105	0.760	25.92	19.31
8	ε_μ	0.046	0.098	0.078	0.078	0.103
	ε_σ	0.020	0.029	0.039	0.021	0.032
	T_{tr}	3.221	0.102	0.771	19.95	19.83
9	ε_μ	0.036	0.095	0.073	0.076	0.091
	ε_σ	0.026	0.028	0.037	0.021	0.020
	T_{tr}	3.256	0.100	0.770	23.53	19.18

hours). This significant speed-up, coupled with high accuracy, underscores the computational efficiency and effectiveness of our solver-free, amortized training strategy for large-scale, complex dynamical systems. While SINDy-based methods train faster than PNODE/PNSDE, their accuracy remains notably lower than our approach for this problem.

Visualizations of the predictions and error statistics of our stochastic ROM are provided in Figures 5 and 6. Similar to the reaction-diffusion system, the mean error for our approach grows approximately linearly over time, starting at 0.01 and reaching around 0.06 by the end of the simulation period. This is mainly due to the same reason discussed earlier: the ROM slowly drifts out of phase with the true solution. The prediction snapshots for a sample test trajectory show that the prediction uncertainty is initially uniform but becomes more pronounced in the cylinder wake as errors accumulate, aligning with regions of complex flow dynamics. See movie S4 for a visualization of the prediction error over time.

4 Discussion

In this work, we have developed a powerful new approach for constructing stochastic ROMs that captures the dependence of the dynamics on system parameters and forcing conditions while enabling joint inference of the ROM along with a probabilistic autoencoder. By eliminating forward solvers from the training process, we achieve a significant breakthrough in computational efficiency and advance the state-of-the-art in data-driven ROM methodology. The amortized SVI framework decouples the training cost from the number of training trajectories, time-step resolution, and system stiffness. This enables efficient distillation of complex relationships between the dynamics, system parameters, and time-dependent forcing from large-scale datasets.

Our approach offers unique flexibility in model construction. While we can learn parsimonious latent models comparable to those obtained using SINDy [24], we do so without requiring time derivatives in the training data. This represents a significant practical advantage since numerical differentiation often amplifies measurement noise. Indeed, the reaction-diffusion test case – where noise was added independently to state samples and their time derivatives – represents an ideal scenario for SINDy’s performance on noisy datasets.

Even though our amortized construction of the latent variational distribution offers substantial computational advantages over existing approaches, the ELBO evaluation cost remains a limiting factor. Further computational efficiency gains would enable application to even more demanding problems, such as high-resolution atmospheric modeling [44] and learning dynamical systems from large-scale neural activity datasets [45].

Our implementation demonstrates only a subset of possible statistical priors for enhancing ROM performance. Future work could incorporate domain knowledge by encoding physical features – such as dissipation or oscillation patterns – into specialized parametrizations of the latent drift function. For systems with known FOMs, Galerkin projection could inform stronger priors on the latent SDE, potentially improving

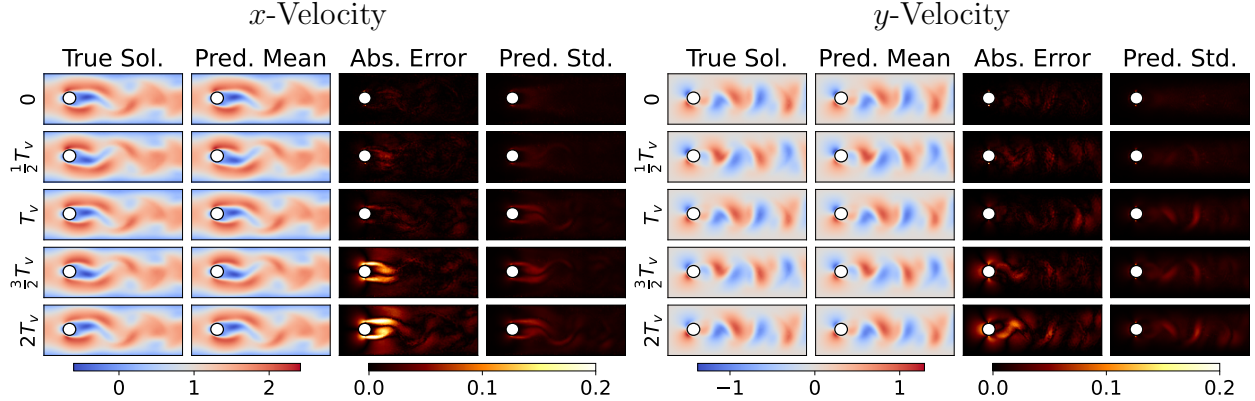


Figure 5: Fluid flow with control: solution, error, & prediction statistics for a test trajectory. Only the velocity field on the left half of the domain is shown. See movie S4.

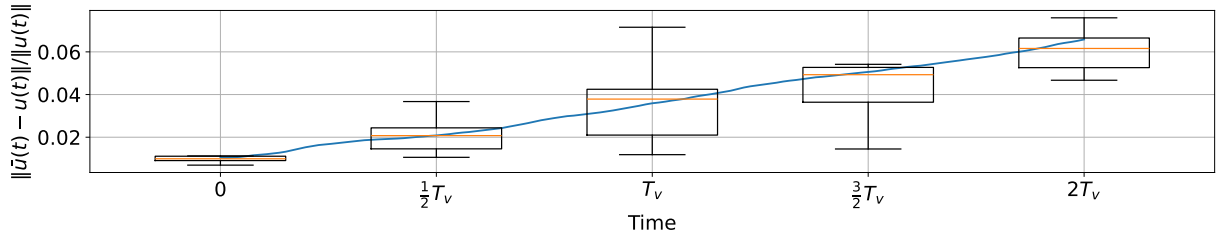


Figure 6: Fluid flow with control: error distribution on test set over time for $d = 9$.

both training efficiency and model interpretability.

The methodology presented here bridges the spectrum between physics-driven and data-driven ROM. Although our focus has been primarily on the data-driven end – working with time-series data corresponding to variations in parameters and forcing without access to the FOM – our framework’s ability to incorporate known physics makes it adaptable across this entire spectrum. More specifically, the ability to incorporate full or partial statistical priors derived from structural or physical assumptions provides a natural bridge between purely data-driven and physics-informed modeling paradigms. This versatility also opens up exciting new possibilities for tackling challenging problems such as probabilistic coarse-grained modeling [46], learning Koopman representations [47] of complex dynamical systems, and inferring models from indirect observations [33, 48], positioning our approach as a foundational tool for scientific machine learning.

Data/code availability A software library implementing the proposed stochastic ROM methodology along with training and evaluation datasets to reproduce our results is available on GitHub: <https://github.com/ailersic/rom-visde>.

Acknowledgments This research is supported by an NSERC Discovery Grant, a Queen Elizabeth II Graduate Scholarship in Science and Technology, and a grant from the Data Sciences Institute at the University of Toronto.

References

[1] Richard L. Fox and Hirokazu Miura. An approximate analysis technique for design calculations. *AIAA Journal*, 9(1):177–179, 1971.

[2] Peter Benner, Wil Schilders, Stefano Grivet-Talocia, Alfio Quarteroni, Gianluigi Rozza, and Luís Miguel Silveira. *Model order reduction*, volume 1-3. De Gruyter, Berlin, 2022.

[3] Benjamin Peherstorfer. Breaking the Kolmogorov barrier with nonlinear model reduction. *Notices of the American Mathematical Society*, 69(5):725–733, 2022.

[4] Christophe Audouze, Florian De Vuyst, and Prasanth B. Nair. Reduced-order modeling of parameterized PDEs using time–space-parameter principal component analysis. *International Journal for Numerical Methods in Engineering*, 80(8):1025–1057, 2009.

[5] Christophe Audouze, Florian De Vuyst, and Prasanth B. Nair. Nonintrusive reduced-order modeling of parametrized time-dependent partial differential equations. *Numerical Methods for Partial Differential Equations*, 29(5):1587–1628, 2013.

[6] Benjamin Peherstorfer and Karen Willcox. Data-driven operator inference for nonintrusive projection-based model reduction. *Computer Methods in Applied Mechanics and Engineering*, 306:196–215, 2016.

[7] Shane A. McQuarrie, Parisa Khodabakhshi, and Karen E. Willcox. Nonintrusive reduced-order models for parametric partial differential equations via data-driven operator inference. *SIAM Journal on Scientific Computing*, 45(4):A1917–A1946, 2023.

[8] Zhong Yi Wan, Pantelis Vlachas, Petros Koumoutsakos, and Themistoklis Sapsis. Data-assisted reduced-order modeling of extreme events in complex dynamical systems. *PLOS ONE*, 13(5):1–22, 05 2018.

[9] Wei W. Xing, Akeel A. Shah, and Prasanth B. Nair. Reduced dimensional Gaussian process emulators of parametrized partial differential equations based on isomap. *Proceedings of the Royal Society A: Mathematical, Physical and Engineering Sciences*, 471(20140697), 2015.

[10] Wei W. Xing, Vasileios Triantafyllidis, Akeel A. Shah, Prasanth B. Nair, and Nicholas Zabaras. Manifold learning for the emulation of spatial fields from computational models. *Journal of Computational Physics*, 326:666–690, 2016.

[11] Jiayang Xu and Karthik Duraisamy. Multi-level convolutional autoencoder networks for parametric prediction of spatio-temporal dynamics. *Computer Methods in Applied Mechanics and Engineering*, 372:113379, 2020.

[12] Kookjin Lee and Kevin T. Carlberg. Model reduction of dynamical systems on nonlinear manifolds using deep convolutional autoencoders. *Journal of Computational Physics*, 404:108973, 2020.

[13] Youngkyu Kim, Youngsoo Choi, David Widemann, and Tarek Zohdi. A fast and accurate physics-informed neural network reduced order model with shallow masked autoencoder. *Journal of Computational Physics*, 451:110841, 2022.

[14] Romit Maulik, Bethany Lusch, and Prasanna Balaprakash. Reduced-order modeling of advection-dominated systems with recurrent neural networks and convolutional autoencoders. *Physics of Fluids*, 33(3):037106, 2021.

[15] Joshua Barnett and Charbel Farhat. Quadratic approximation manifold for mitigating the Kolmogorov barrier in nonlinear projection-based model order reduction. *Journal of Computational Physics*, 464:111348, 2022.

[16] Francesco Romor, Giovanni Stabile, and Gianluigi Rozza. Nonlinear manifold reduced-order models with convolutional autoencoders and reduced over-collocation method. *Journal of Scientific Computing*, 94(3), 2023.

[17] Cheng Huang and Karthik Duraisamy. Predictive reduced order modeling of chaotic multi-scale problems using adaptively sampled projections. *Journal of Computational Physics*, 491:112356, 2023.

[18] Ricardo Baptista, Youssef Marzouk, and Olivier Zahm. Gradient-based data and parameter dimension reduction for Bayesian models: an information theoretic perspective. *arXiv preprint*, 2022.

- [19] P. Benner, S. Gugercin, and K. Willcox. A survey of projection-based model reduction methods for parametric dynamical systems. *SIAM Review*, 57(4), 2015.
- [20] William D. Fries, Xiaolong He, and Youngsoo Choi. LaSDI: Parametric latent space dynamics identification. *Computer Methods in Applied Mechanics and Engineering*, 399:115436, 2022.
- [21] Junming Duan and Jan S. Hesthaven. Non-intrusive data-driven reduced-order modeling for time-dependent parametrized problems. *Journal of Computational Physics*, 497:112621, 2024.
- [22] Emilien Dupont, Arnaud Doucet, and Yee Whye Teh. Augmented neural ODEs. *Advances in Neural Information Processing Systems*, 32, 2019.
- [23] Kookjin Lee and Eric J. Parish. Parameterized neural ordinary differential equations: applications to computational physics problems. *Proceedings of the Royal Society A: Mathematical, Physical and Engineering Sciences*, 477(2253):20210162, 2021.
- [24] Kathleen Champion, Bethany Lusch, J. Nathan Kutz, and Steven L. Brunton. Data-driven discovery of coordinates and governing equations. *Proceedings of the National Academy of Sciences*, 116(45):22445–22451, 2019.
- [25] Julius Aka, Johannes Brunnemann, Jörg Eiden, Arne Speerforck, and Lars Mikelsons. Balanced neural ODEs: nonlinear model order reduction and Koopman operator approximations. *arXiv preprint*, 2025.
- [26] George Karniadakis, Ali Beskok, and Narayan Aluru. *Microflows and Nanoflows Fundamentals and Simulation*. Interdisciplinary Applied Mathematics, 29. Springer, New York, NY, 1st edition, 2005.
- [27] Daniel T. Gillespie. Stochastic simulation of chemical kinetics. *Annual Review of Physical Chemistry*, 58(Volume 58, 2007):35–55, 2007.
- [28] Christopher V. Rao, Denise M. Wolf, and Adam P. Arkin. Control, exploitation and tolerance of intracellular noise. *Nature*, 420(6912):231–237, Nov 2002.
- [29] Cédric Archambeau, Dan Cornford, Manfred Opper, and John Shawe-Taylor. Gaussian process approximations of stochastic differential equations. *Gaussian Processes in Practice*, 1:1–16, 12–13 Jun 2007.
- [30] Cédric Archambeau, Manfred Opper, Yuan Shen, Dan Cornford, and John Shawe-taylor. Variational inference for diffusion processes. *Advances in Neural Information Processing Systems*, 20, 2007.
- [31] Xuechen Li, Ting-Kam Leonard Wong, Ricky T. Q. Chen, and David K. Duvenaud. Scalable gradients and variational inference for stochastic differential equations. *Proceedings of The 2nd Symposium on Advances in Approximate Bayesian Inference*, 118:1–28, 08 Dec 2020.
- [32] Patrick Kidger. On neural differential equations. *arXiv preprint*, 2022.
- [33] Kevin Course and Prasanth B. Nair. State estimation of a physical system with unknown governing equations. *Nature*, 622(7982):261–267, Oct 2023.
- [34] Kevin Course and Prasanth B. Nair. Amortized reparametrization: Efficient and scalable variational inference for latent SDEs. *Advances in Neural Information Processing Systems*, 36:78296–78318, 2023.
- [35] Simo Särkkä and Arno Solin. *Applied stochastic differential equations*, volume 10 of *Institute of Mathematical Statistics Textbooks*. Cambridge University Press, Cambridge, 2019.
- [36] Diederik P. Kingma and Max Welling. Auto-encoding variational Bayes. *arXiv preprint*, 2022.
- [37] Jean Rabault, Miroslav Kuchta, Atle Jensen, Ulysse Réglade, and Nicolas Cerardi. Artificial neural networks trained through deep reinforcement learning discover control strategies for active flow control. *Journal of Fluid Mechanics*, 865:281–302, 2019.

[38] Paolo Conti, Giorgio Gobat, Stefania Fresca, Andrea Manzoni, and Attilio Frangi. Reduced order modeling of parametrized systems through autoencoders and sindy approach: continuation of periodic solutions. *Computer Methods in Applied Mechanics and Engineering*, 411:116072, 2023.

[39] Zachary G. Nicolaou, Guanyu Huo, Yihui Chen, Steven L. Brunton, and J. Nathan Kutz. Data-driven discovery and extrapolation of parameterized pattern-forming dynamics. *Phys. Rev. Res.*, 5:L042017, Nov 2023.

[40] Brian de Silva, Kathleen Champion, Markus Quade, Jean-Christophe Loiseau, J. Kutz, and Steven Brunton. Pysindy: A python package for the sparse identification of nonlinear dynamical systems from data. *Journal of Open Source Software*, 5(49):2104, 2020.

[41] Alan A. Kaptanoglu, Brian M. de Silva, Urban Fasel, Kadierdan Kaheman, Andy J. Goldschmidt, Jared Callaham, Charles B. Delahunt, Zachary G. Nicolaou, Kathleen Champion, Jean-Christophe Loiseau, J. Nathan Kutz, and Steven L. Brunton. Pysindy: A comprehensive python package for robust sparse system identification. *Journal of Open Source Software*, 7(69):3994, 2022.

[42] Ricky T. Q. Chen, Yulia Rubanova, Jesse Bettencourt, and David Duvenaud. Neural ordinary differential equations. In *Proceedings of the 32nd International Conference on Neural Information Processing Systems*, NIPS'18, page 6572–6583, Red Hook, NY, USA, 2018. Curran Associates Inc.

[43] Yulia Rubanova, Ricky T. Q. Chen, and David K Duvenaud. Latent ordinary differential equations for irregularly-sampled time series. *Advances in Neural Information Processing Systems*, 32, 2019.

[44] Sungduk Yu, Zeyuan Hu, Akshay Subramaniam, Walter Hannah, Liran Peng, Jerry Lin, Mohamed Aziz Bhouri, Ritwik Gupta, Björn Lütjens, Justus C. Will, Gunnar Behrens, Julius J. M. Busecke, Nora Loose, Charles I. Stern, Tom Beucler, Bryce Harrop, Helge Heuer, Benjamin R. Hillman, Andrea Jenney, Nana Liu, Alistair White, Tian Zheng, Zhiming Kuang, Fiaz Ahmed, Elizabeth Barnes, Noah D. Brenowitz, Christopher Bretherton, Veronika Eyring, Savannah Ferretti, Nicholas Lutsko, Pierre Gentine, Stephan Mandt, J. David Neelin, Rose Yu, Laure Zanna, Nathan Urban, Janni Yuval, Ryan Abernathey, Pierre Baldi, Wayne Chuang, Yu Huang, Fernando Iglesias-Suarez, Sanket Jantre, Po-Lun Ma, Sara Shamekh, Guang Zhang, and Michael Pritchard. ClimSim-Online: a large multi-scale dataset and framework for hybrid ML-physics climate emulation. *arXiv preprint*, 2024.

[45] Mehdi Azabou, Vinam Arora, Venkataramana Ganesh, Ximeng Mao, Santosh Nachimuthu, Michael Mendelson, Blake Richards, Matthew Perich, Guillaume Lajoie, and Eva L. Dyer. A unified, scalable framework for neural population decoding. *Advances in Neural Information Processing Systems*, 2023.

[46] Jiang Wang, Simon Olsson, Christoph Wehmeyer, Adrià Pérez, Nicholas E. Charron, Gianni de Fabritiis, Frank Noé, and Cecilia Clementi. Machine learning of coarse-grained molecular dynamics force fields. *ACS Central Science*, 5(5):755–767, May 2019.

[47] Steven L. Brunton, Marko Budišić, Eurika Kaiser, and J. Nathan Kutz. Modern Koopman theory for dynamical systems. *SIAM Review*, 64(2):229–340, 2022.

[48] Maziar Raissi, Alireza Yazdani, and George Em Karniadakis. Hidden fluid mechanics: Learning velocity and pressure fields from flow visualizations. *Science*, 367(6481):1026–1030, 2020.

[49] Ricky T. Q. Chen. torchdiffeq: PyTorch implementation of differentiable ODE solvers. <https://github.com/rtqichen/torchdiffeq>, 2018.

[50] YongKyung Oh, Dongyoung Lim, and Sungil Kim. Stable neural stochastic differential equations in analyzing irregular time series data. In *The Twelfth International Conference on Learning Representations*, 2024.

[51] Peter Craigmire, Radu Herbei, Ge Liu, and Grant Schneider. Statistical inference for stochastic differential equations. *WIREs Computational Statistics*, 15(2):e1585, 2023.

[52] Grigori N. Milstein. A method of second-order accuracy integration of stochastic differential equations. *Theory of Probability & Its Applications*, 23(2):396–401, 1979.

[53] Ola Elerian. A note on the existence of a closed form conditional transition density for the Milstein scheme. *Economics discussion paper*, page W18, 1998.

[54] Yacine Aït-Sahalia. Maximum likelihood estimation of discretely sampled diffusions: A closed-form approximation approach. *Econometrica*, 70(1):223–262, 2002.

[55] John C. Cox, Jonathan E. Ingersoll, and Stephen A. Ross. A theory of the term structure of interest rates. *Econometrica*, 53(2):385–407, 1985.

[56] George E. Uhlenbeck and Leonard S. Ornstein. On the theory of the Brownian motion. *Phys. Rev.*, 36:823–841, Sep 1930.

[57] Alexandros Beskos and Gareth O. Roberts. Exact simulation of diffusions. *The Annals of Applied Probability*, 15:2422–2444, 2005.

[58] Jose Blanchet and Fan Zhang. Exact simulation for multivariate Itô diffusions. *Advances in Applied Probability*, 52(4):pp. 1003–1034, 2020.

[59] Ben Mildenhall, Pratul P. Srinivasan, Matthew Tancik, Jonathan T. Barron, Ravi Ramamoorthi, and Ren Ng. Nerf: Representing scenes as neural radiance fields for view synthesis. In *European Conference on Computer Vision (ECCV)*, 2020.

[60] Matthew Tancik, Pratul P. Srinivasan, Ben Mildenhall, Sara Fridovich-Keil, Nithin Raghavan, Utkarsh Singhal, Ravi Ramamoorthi, Jonathan T. Barron, and Ren Ng. Fourier features let networks learn high frequency functions in low dimensional domains. *NeurIPS*, 2020.

[61] William Falcon and The PyTorch Lightning team. PyTorch Lightning. <https://github.com/rtqichen/torchdiffeq>, March 2019.

[62] Diederik P. Kingma and Jimmy Ba. Adam: A method for stochastic optimization. *arXiv preprint*, 2017.

[63] Anders Logg, Garth Wells, and Kent-Andre Mardal. *Automated Solution of Differential Equations by the Finite Element Method: The FEniCS Book*, volume 84 of *Lecture Notes in Computational Science and Engineering*. Springer, Berlin, Heidelberg, April 2011.

A PNODE/PNSDE details

In this section, we summarize the PNODE and PNSDE baseline models used in this work.

PNODE formulation In the original PNODE formulation of Lee and Parish [23], the forward pass proceeds as follows. For the i th trajectory with parameters μ_i and initial condition $u_i(0)$: (1) the latent initial condition is obtained from a deterministic encoder $z_i(0) = h_\theta^{\text{enc}}(u_i(0))$; (2) the parametrized neural ODE $z_i(t) = z_i(0) + \int_0^t \psi_\theta(z, t; \mu_i) dt$ is solved forward in time for a drift function ψ_θ ; and (3) the latent solution is mapped through a deterministic decoder to obtain the prediction $\bar{u}_i(t) = h_\theta^{\text{dec}}(z_i(t))$. The parameters θ (encoder, decoder, and drift) are originally learned by minimizing the mean-squared error

$$\mathcal{L}(\theta) = \frac{1}{N_T} \sum_{i=1}^{N_T} \frac{1}{N_i} \sum_{j=1}^{N_i} (u_{i,j} - \bar{u}_i(t_j))^2.$$

In our numerical experiments, this MSE loss was not sufficient for large multi-trajectory datasets, as it does not impose a prior over the latent state. We therefore replace the MSE loss with an ELBO using a prior $p(z)$ on the latent state, as in variational autoencoders [36], which has previously been used for training latent neural ODE models [49, 43]:

$$\mathcal{L}(\theta) = \sum_{i=1}^{N_T} \sum_{j=1}^{N_i} \mathbb{E}_{z_{i,j}} [\log p_\theta^{\text{dec}}(u_i(t_{i,j}; \mu_i) | z_{i,j})] - \sum_{i=1}^{N_T} D_{\text{KL}}(p_\theta^{\text{enc}}(z_i(0) | \mu_i) \| p(z)),$$

where $p_\theta^{\text{enc}}(z_i(0) | \mu_i)$ is the initial-condition encoder, $p(z) = \mathcal{N}(0, I)$, and

$$z_{i,j} = z_i(0) + \int_0^{t_{i,j}} \psi_\theta(z, t; \mu_i) dt, \quad z_i(0) \sim p_\theta^{\text{enc}}(z_i(0) | \mu_i).$$

Using an ELBO requires probabilistic encoders and decoders rather than deterministic ones, so we adopt probabilistic versions of these components. The encoder, decoder, and drift share the same neural architectures as the corresponding modules in our proposed approach for each example.

In our numerical experiments, the PNODE model trained by maximizing the ELBO yields better generalization performance. For example, on the Burgers' equation dataset (see Example 2 in Section 3) with ROM dimension $d = 3$, the PNODE model attains a mean test error of 0.075 with the ELBO, compared with 0.135 when trained with the MSE loss.

PNSDE formulation Neural SDEs form a broad class of dynamical models [50]. Our PNSDE baseline is obtained as a straightforward extension of the PNODE formulation. Retaining the same ELBO and model architecture, we augment the latent dynamics with a dispersion term:

$$z_{i,j} \sim z_i(0) + \int_0^{t_{i,j}} \psi_\theta(z, t; \mu_i) dt + \int_0^{t_{i,j}} \Psi_\theta(t; \mu_i) d\beta, \quad z_i(0) \sim p_\theta^{\text{enc}}(z_i(0) | \mu_i), \quad (14)$$

which is almost identical to the SDE prior in (1), except that it omits time-dependent forcing. Because the dynamics depend on parameters μ , we refer to this baseline as a parametrized neural SDE (PNSDE) model.

Parametric inference of θ in this formulation introduces a theoretical complication. Evaluating the log-likelihood term in the ELBO requires the distribution of the latent state z , induced by the stochastic process in (14). The associated transition density $q(z(t) | t, z(0))$, which satisfies the Fokker–Planck equation, typically does not admit a closed form for general SDE systems, so the log-likelihood cannot be evaluated exactly.² There is extensive literature on approximations of the transition density and on special cases with closed-form solutions; see Craigmire et al. [51] for a recent overview.

²This limitation does not arise in the SVI-based approach proposed in this work, despite its use of a latent SDE model, because the latent variational distribution over z is parametrized as a linear Markov Gaussian process, rather than as a realization of an arbitrary stochastic process.

For the PNSDE baseline, we adopt an approximate transition density obtained from the Euler–Maruyama time-marching scheme,

$$z(t + \Delta t) = z(t) + \psi_\theta(z(t), t; \mu) \Delta t + \Psi_\theta(t; \mu) \Delta \beta,$$

where Δt is the time step and $\Delta \beta \sim \mathcal{N}(0, \Delta t I)$. Given $z(t)$ at time t , this yields a Gaussian stepwise transition density for $z(t + \Delta t)$,

$$q(z(t + \Delta t) | \Delta t, z(t)) = \mathcal{N}(z(t) + \psi_\theta(z(t), t; \mu) \Delta t, \Psi_\theta(t; \mu) \Psi_\theta^\top(t; \mu) \Delta t),$$

which we then use to approximate the full-trajectory transition density over $[0, t]$. Given an initial condition $z(0)$, a final time t , and time step Δt such that $t = N\Delta t$ for $N \in \mathbb{Z}$,

$$q(z(t) | t, z(0)) = \prod_{j=1}^N q(z(t_j) | \Delta t, z(t_{j-1})), \quad \text{where } t_j = j\Delta t, t_0 = 0,$$

which serves as our transition-density approximation.

Other time-marching schemes admit analogous approximate closed-form transition densities, including the Milstein method [52, 53] and the Aït-Sahalia method [54]. Such approximations are, in practice, the only viable option for obtaining closed-form transition densities while retaining a flexible neural parametrization of the SDE. One may instead restrict attention to SDE families with known closed-form transition densities, such as the Cox–Ingwersoll–Ross model [55] or the Ornstein–Uhlenbeck process [56], but these do not admit neural parametrizations. A more general alternative is exact simulation of SDEs via rejection sampling, as in the methods of Beskos and Roberts [57] for univariate systems and Blanchet and Zhang [58] for multivariate systems, but their computational cost is prohibitive (the expected termination time is infinite in the latter), and they are therefore not practical for tackling the class of problems considered in the present work.

B Summary of parametrized terms

We summarize below all components of the proposed stochastic ROM framework with learnable parameters.

The variational encoder The variational encoder $p_\theta^{\text{enc}}(z(t) | u(t)) := \mathcal{N}(m_z, S_z)$ involves two parametrized terms: a mean function that maps the QoI $u(t) \in \mathbb{R}^D$ to the mean of the latent state $m_z \in \mathbb{R}^d$, and a variance function that maps the QoI $u(t) \in \mathbb{R}^D$ to the variance of the latent state $s_z \in \mathbb{R}^d$, such that $S_z = \text{diag}(s_z)$. Note that in this definition, the covariance S_z is parametrized as a diagonal matrix.

The variational decoder The variational decoder $p_\theta^{\text{dec}}(u(t) | z(t)) := \mathcal{N}(m_u, S_u)$ also involves two parametrized terms: a mean function that maps the latent state $z(t) \in \mathbb{R}^d$ to the mean of the QoI $m_u \in \mathbb{R}^D$, and a variance function that maps the latent state $z(t) \in \mathbb{R}^d$ to the variance of the QoI $s_u \in \mathbb{R}^d$, such that $S_u = \text{diag}(s_u)$. As with the encoder, in this definition, the covariance S_u is parametrized as a diagonal matrix.

The SDE prior The latent SDE prior, $dz = \psi_\theta(z, t; \mu, f(t))dt + \Psi_\theta(t; \mu)d\beta$, also involves two parametrized terms: a drift function $\psi_\theta : \mathbb{R}^d \times [0, T] \times \mathbb{R}^L \times \mathbb{R}^F \rightarrow \mathbb{R}^d$, and a dispersion matrix $\Psi_\theta : [0, T] \times \mathbb{R}^L \rightarrow \mathbb{R}^d$. In all our numerical studies, we use feedforward neural networks with ReLU activation to represent ψ_θ and Ψ_θ . We apply the transformation $t \mapsto (\sin(2\pi t), \cos(2\pi t)) \in \mathbb{R}^2$ to the time variable t and provide this feature vector as input to the feedforward neural network parametrizing the drift function. This feature space map is sometimes referred to as a “positional encoding” and widely used to overcome the spectral bias of coordinate-based feedforward neural networks; for a detailed discussion, see [59, 60].

The amortized variational distribution The amortized variational distribution, $q_\phi(z | t; \mu_i, f_i, \mathcal{D}_{i,k})$, is parametrized using a deep kernel model with learnable parameters σ, σ_f, ℓ , and the weights and biases of the feedforward neural network φ ; see Section 2.5. This kernel maps from two time samples $t_1, t_2 \in \mathbb{R}$ to a similarity measure $\kappa(t_1, t_2) \in \mathbb{R}$.

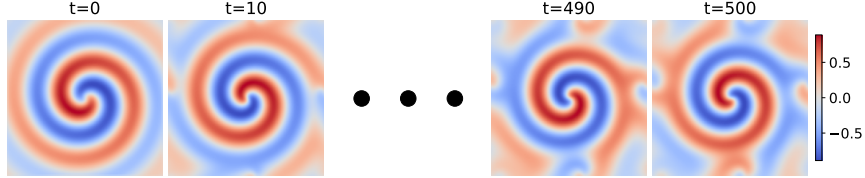


Figure 7: Reaction-diffusion: snapshots of solution over the whole time domain.

C Details of Example Problems

This section provides additional details for the example problems given in Section 3. For each case, we also describe the model architecture and the training settings. All the numerical studies were carried out on an Ubuntu server with a dual Intel Xeon E5-2680 v3 with a total of 24 cores, 128GB of RAM, and an Nvidia GeForce RTX 4090 GPU. PyTorch Lightning [61] was used to implement the proposed stochastic ROM methodology, and the code along with test cases are available on our GitHub repository: <https://github.com/ailersic/visde>. In all the numerical studies, we use an amortized variational distribution for the latent state z . If prior distributions are specified for certain model parameters θ , we learn variational distributions over those as well; if not, we obtain point estimates.

We provide associated movies for each example problem as supplementary material to this paper, showing model predictions and error.

C.1 Reaction-Diffusion System in 2D

The first example is the reaction-diffusion system taken from Champion et al. [24] and given by a coupled system of PDEs,

$$\begin{aligned} v_t &= (1 - (v^2 + w^2))v + \beta(v^2 + w^2)w + \lambda(v_{xx} + v_{yy}) \\ w_t &= (1 - (v^2 + w^2))w - \beta(v^2 + w^2)v + \lambda(w_{xx} + w_{yy}), \end{aligned}$$

with $(x, y, t) \in [-10, 10] \times [-10, 10] \times [0, 500]$, $\lambda = 0.1$, and $\beta = 1$. The initial condition is given by

$$\begin{aligned} v(x, y, 0) &= \tanh\left(\sqrt{x^2 + y^2} \cos\left(\angle(x + iy) - \sqrt{x^2 + y^2}\right)\right) \\ w(x, y, 0) &= \tanh\left(\sqrt{x^2 + y^2} \sin\left(\angle(x + iy) - \sqrt{x^2 + y^2}\right)\right), \end{aligned}$$

where i is the imaginary unit. The solution is shown in Figure 7. This is an unparametrized and unforced test case, so μ and f do not appear. Only v is recorded in the dataset.

The spatial domain is discretized using a grid with $D = 100 \times 100$ equispaced points, and the time domain is discretized using 9999 steps. We consider a single trajectory, and the time interval is partitioned as follows: the interval $[0, 400]$ constitutes the training set, the next interval $(400, 450]$ is the validation set, and the final $(450, 500]$ is the test set. We set up the training data in a manner identical to Champion et al., except that whereas they corrupt the training data (both v and its time derivative v_t , independently) using zero-mean Gaussian noise with standard deviation 10^{-6} , we consider two cases: a noiseless case, and a noisy case with standard deviation 10^{-2} .

To enable direct comparison with Champion et al.'s approach (which combines an autoencoder with a sparse latent ODE), we represent our drift term ψ_θ as a third-order polynomial and use a $d = 2$ -dimensional latent state. We do not modify the SINDy model architecture and use their suggested training protocol (3000 epochs plus 1000 refinement epochs). We train our stochastic ROM for 1000 epochs.

For the latent SINDy baselines, we have two primary hyperparameters to choose: the order of the polynomial basis, and the thresholding on the coefficients. To choose the threshold, we conduct a grid search over $\{0.001, 0.003, 0.01, 0.03, 0.1\}$ and choose the value that minimizes mean error ε_μ over the validation set. The polynomial order is chosen to be 3 following Champion et al. [24]. Hyperparameters that led to unstable models on the validation set were disqualified. The chosen hyperparameters are shown in Table 4.

Table 4: Reaction-diffusion: hyperparameter combinations chosen for latent SINDy models to minimize validation error.

Dataset	POD-SINDy		AE-SINDy	
	Poly. order	Threshold	Poly. order	Threshold
Noiseless	3	0.1	3	0.03
Noisy	3	0.1	3	0.1

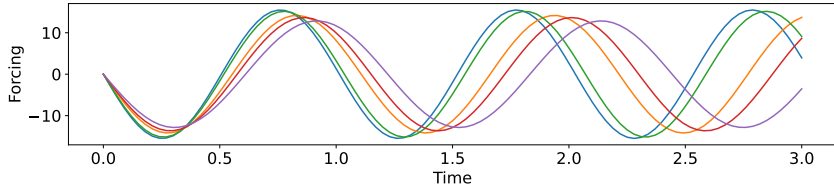


Figure 8: Burgers' equation: five samples of the forcing function f in the training set.

Architecture and Training The encoder mean is a CNN that takes u as the input with the following architecture:

$$\begin{aligned} \text{Conv}[1, 8] &\xrightarrow{\text{ReLU}} \text{Conv}[8, 16] \xrightarrow{\text{ReLU}} \text{Conv}[16, 32] \xrightarrow{\text{ReLU}} \\ &\text{Conv}[32, 64] \xrightarrow{\text{ReLU}} \text{Conv}[64, 128] \xrightarrow{\text{ReLU}} \text{Linear}[n_h, d] \end{aligned}$$

where for all convolutional layers, stride is 2, padding is 2, and kernel size is 5. Note that the first layer takes a 3-channel input, as this dataset includes 2D velocity and pressure fields. The hidden dimension consequently becomes $n_h = 2048$ for this setting of the convolution layers. The architecture of the decoder mean is defined in a symmetric manner using transposed convolution layers as follows:

$$\begin{aligned} \text{Linear}[d, n_h] &\xrightarrow{\text{ReLU}} \text{ConvT}[128, 64] \xrightarrow{\text{ReLU}} \text{ConvT}[64, 32] \xrightarrow{\text{ReLU}} \\ &\text{ConvT}[32, 16] \xrightarrow{\text{ReLU}} \text{ConvT}[16, 8] \xrightarrow{\text{ReLU}} \text{ConvT}[8, 1]. \end{aligned}$$

Output padding is used to recover the state dimension D . The encoder variance and decoder variance are parametrized directly, such that they are constant with respect to u and z , respectively.

For this test case, the drift function is parametrized as a third-order polynomial of the latent state $z \in \mathbb{R}^d$ with $d = 2$, i.e.,

$$\phi_\theta(z, t; \mu, f(t)) = \theta_1 + \theta_2 z_1 + \theta_3 z_2 + \theta_4 z_1^2 + \theta_5 z_1 z_2 + \theta_6 z_2^2 + \theta_7 z_1^3 + \theta_8 z_1^2 z_2 + \theta_9 z_1 z_2^2 + \theta_{10} z_2^3,$$

where $\theta_i \in \mathbb{R}^d$, $i = 1, 2, \dots, 10$ leading to $\theta \in \mathbb{R}^{10d}$ parameters in total. The parameters μ and forcing $f(t)$ are not relevant in this example, so they are not included in the drift. The dispersion matrix is, like the variance of the encoder/decoder, parametrized directly, making it constant with respect to t and μ .

A log-normal prior is placed on the variance of the decoder, or equivalently, a normal prior is placed on the log-variance. This is to ensure that all components of the decoder variance stay within a similar order-of-magnitude range, which in turn reduces the variance in the gradient of the ELBO's log-likelihood term (see (3)).

Finally, the deep kernel (see Section 2.5) applies the neural network $\varphi(t)$ to each input, which is defined as

$$\text{Linear}[1, 128] \xrightarrow{\text{ReLU}} \text{Linear}[128, 128] \xrightarrow{\text{ReLU}} \text{Linear}[128, 1].$$

For this model, we train with the Adam optimizer [62] with an initial learning rate of 3×10^{-3} for 1000 epochs and a batch size of 128. We use an exponential decay scheduler, such that the learning rate decays by 10% every 2000 iterations.

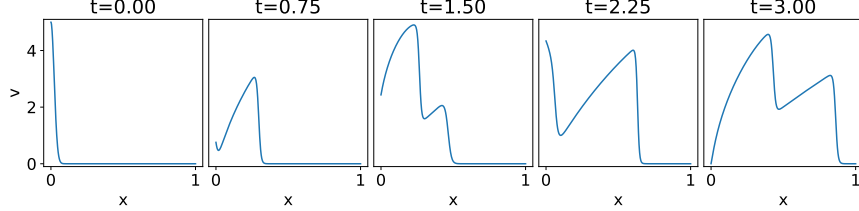


Figure 9: Burgers' equation: snapshots of solution over the whole time domain.

Interpretable dynamics The strength of using SINDy for a problem like this is its ability to learn *interpretable* dynamics. Champion et al. [24] reported the following linear latent system,

$$\dot{z}_1 = -0.85z_2 \quad \dot{z}_2 = 0.97z_1,$$

that lays bare the periodic nature of the dynamics. For each noisy/noiseless variant of the dataset, a similar linear system is discovered.³ By using the same polynomial form for our drift function, we are able to recover similar linear dynamics. The drift function learned by our approach for the noiseless dataset is shown below:

$$\begin{aligned} \psi_\theta(z, t; \mu, f(t)) &= 10^{-2} \times \begin{bmatrix} -3.7 & 3.9 & 93 & -0.90 & -0.33 & -2.5 & -0.33 & 0.10 & -0.44 & 0.29 \\ 2.7 & -89 & -1.9 & 0.37 & -1.0 & -0.48 & 0.24 & -0.50 & 0.33 & -0.51 \end{bmatrix} \begin{bmatrix} 1 \\ z_1 \\ z_2 \\ z_1^2 \\ z_1 z_2 \\ z_2^2 \\ z_1^3 \\ z_1^2 z_2 \\ z_1 z_2^2 \\ z_2^3 \end{bmatrix} \\ &\approx \begin{bmatrix} 0.93z_2 \\ -0.89z_1 \end{bmatrix}. \end{aligned}$$

It can be noted that two of the coefficients are around 100 times larger than the rest. This demonstrates that although our SVI-based approach does not require observations of the time-derivatives like SINDy, or any sparsity-inducing regularization or thresholding, it can yield similar sparse models. As mentioned in Section 2.2, a sparsity-inducing prior [33] can also be used in the proposed methodology to strongly enforce interpretability.

C.2 Forced, parametrized Burgers' equation

The next case is the viscous one-dimensional Burgers' equation, given by

$$v_t = -v v_x + \nu v_{xx}, \quad (x, t) \in [0, 1] \times [0, 3],$$

with the boundary conditions $v(0, t) = f(t)$, $v(1, t) = 0$. The viscosity is parametrized as $\nu \in [0.05, 0.1]$, and $f(t) = \alpha_1 \cos(2\pi\omega t)$ where $\omega \in [0.8, 1]$. The initial condition is $v(x, 0) = \alpha_1 \exp(-x^2/\alpha_2)$, where $\alpha_1 = 5$ and $\alpha_2 = 0.001$.

We discretize the governing equations on a spatial mesh with $D = 500$ equispaced points. We evaluate the spatial derivatives with centered finite-difference operators and use a time marching scheme with $\Delta t = 0.001$ leading to a total of 1001 time samples in each trajectory calculated using the FOM.

The training set consists of 100 trajectories computed for different realizations of $\mu = \nu$ and forcing function f , the validation set consists of 10, and the test set consists of 10. For each trajectory, we randomly

³Note that the coefficient magnitudes are not unique since the autoencoder may allow the latent state to be arbitrarily scaled.

Table 5: Burgers' equation: hyperparameter combinations chosen for latent SINDy models to minimize validation error.

ROM dim.	POD-SINDy		AE-SINDy	
	Poly. order	Threshold	Poly. order	Threshold
$d = 3$	3	0.003	1	0.1
$d = 4$	2	0.03	2	0.1
$d = 5$	3	0.03	3	0.1

sample the viscosity and forcing ω from uniform distributions, i.e., $\nu \sim \mathcal{U}[0.05, 0.1]$ and $\omega \sim \mathcal{U}[0.8, 1]$. Representative realizations of f are shown in Figure 8 and a sample trajectory from the training set is shown in Figure 9. Because the PNODE and PNSDE models do not take the forcing function directly, for those models we include the frequency in the parameters, i.e., $\mu = \{\nu, \omega\}$.

For the latent SINDy baseline, we have two primary hyperparameters to choose: the order of the polynomial basis, and the thresholding on the coefficients. To choose these, we conduct a grid search over polynomial orders $\{1, 2, 3\}$ and thresholds $\{0.001, 0.003, 0.01, 0.03, 0.1\}$ and choose the combination that minimizes mean error ε_μ over the validation set. Hyperparameters that led to unstable models on the validation set were disqualified. The chosen hyperparameters are shown in Table 5.

Architecture and training The CNN architecture of the encoder mean that takes u as the input is given below:

$$\begin{aligned} \text{Conv}[1, 8] &\xrightarrow{\text{ReLU}} \text{Conv}[8, 16] \xrightarrow{\text{ReLU}} \text{Conv}[16, 32] \xrightarrow{\text{ReLU}} \\ \text{Conv}[32, 64] &\xrightarrow{\text{ReLU}} \text{Conv}[64, 128] \xrightarrow{\text{ReLU}} \text{Linear}[n_h, d] \end{aligned}$$

where for all convolutional layers, stride is 2, padding is 2, and kernel size is 5. The hidden dimension comes out to $n_h = 4096$ for this case. The architecture of the decoder mean that takes z as the input is defined in a symmetric manner using transposed convolution layers as follows:

$$\begin{aligned} \text{Linear}[d, n_h] &\xrightarrow{\text{ReLU}} \text{ConvT}[128, 64] \xrightarrow{\text{ReLU}} \text{ConvT}[64, 32] \xrightarrow{\text{ReLU}} \\ \text{ConvT}[32, 16] &\xrightarrow{\text{ReLU}} \text{ConvT}[16, 8] \xrightarrow{\text{ReLU}} \text{ConvT}[8, 1] \end{aligned}$$

Output padding is used to recover the state dimension D . The encoder variance and decoder variance are parametrized directly, such that they are constant with respect to u and z respectively.

As with the previous example, a log-normal prior is placed on the variance of the decoder. To show why this is necessary here, consider that the QoI $u(x, t) \approx 0$ near the right boundary of the x -domain for all t , μ , and $f(t)$. Consequently, when the decoder mean function correctly predicts zero at the boundaries, decreasing the decoder variance causes the log-likelihood term to monotonically increase. Maximizing the ELBO therefore causes the decoder variance to tend to zero. Evaluating the ELBO may then lead to floating-point precision issues, or even a divide-by-zero error.

The drift function is parametrized using a feedforward neural network with ReLU activation that takes the latent state z , the viscosity ν , forcing $f(t)$, and time as inputs,

$$\text{Linear}[n_i, 128] \xrightarrow{\text{ReLU}} \text{Linear}[128, 128] \xrightarrow{\text{ReLU}} \text{Linear}[128, 128] \xrightarrow{\text{ReLU}} \text{Linear}[128, d]$$

where $n_i = d + 1 + N_f + 2 = 13$. Note that the drift does not depend on the FOM initial condition parameters α_1 and α_2 . The term 2 arises due to the feature space map we use for time as described earlier in Section B. The dispersion matrix is, like the variance of the encoder/decoder, parametrized directly, making it constant with respect to t and μ .

Finally, the deep kernel (see Section 2.5) applies the neural network $\varphi(t)$ to each input, which is defined as

$$\text{Linear}[1, 128] \xrightarrow{\text{ReLU}} \text{Linear}[128, 128] \xrightarrow{\text{ReLU}} \text{Linear}[128, 1].$$

For this model and all baseline models, we train using the Adam optimizer [62] with an initial learning rate of 10^{-3} for 50 epochs and a batch size of 64. We use an exponential decay scheduler, such that the learning rate decays by 10% every 2000 iterations.

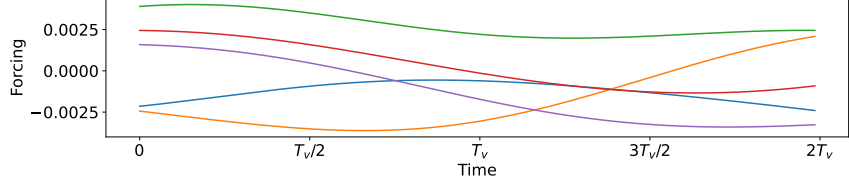


Figure 10: Fluid flow with control: five samples of the forcing function f in the training set.

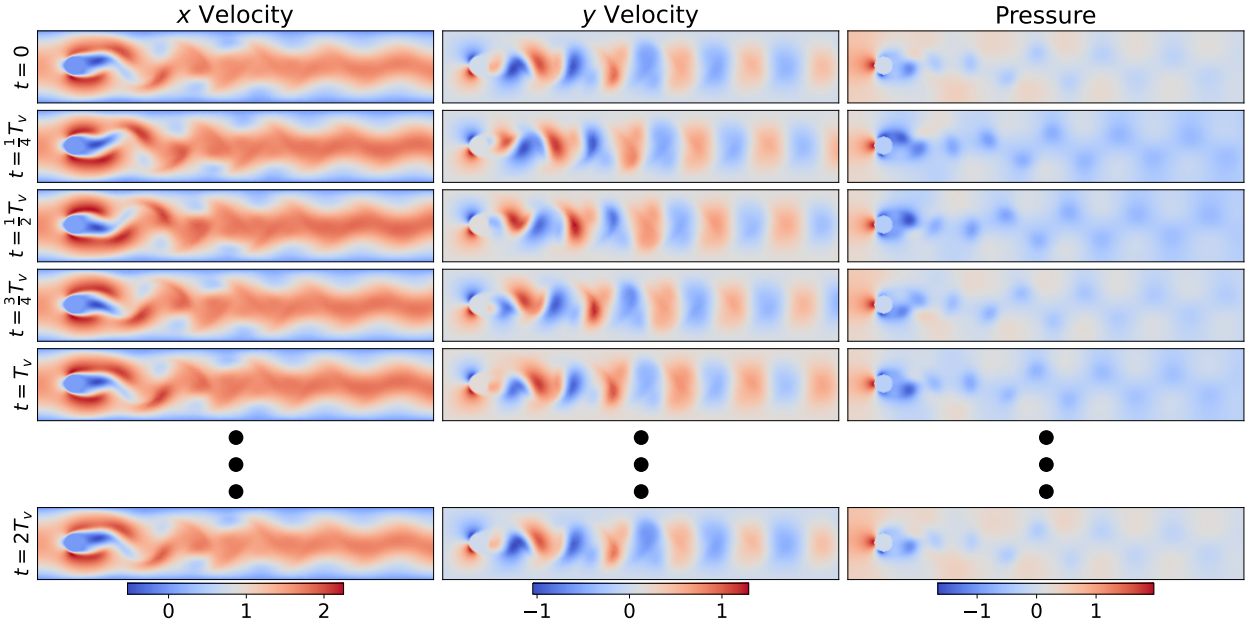


Figure 11: Fluid flow with control: snapshots of solution over the whole time domain.

C.3 Fluid flow with control input

The third example is adapted from the test case involving flow control of a two-dimensional Von Kármán vortex street at $Re = 100$ studied by Rabault et al. [37]. The normalized spatial domain is $x \in [-2, 2.1]$, $y \in [-2, 20]$ and the normalized time domain is $t \in [0, 2]$, which covers $6 \times$ the vortex shedding period $T_v \approx 0.33$. The time domain is discretized into 400 time steps.

The Navier-Stokes equations are solved on an unstructured mesh using FEniCS [63] and the resulting two-dimensional velocity field and scalar pressure field are then resampled onto a 440×80 uniform grid. This gives a state dimension of $D = 440 \times 80 \times 3 = 105,600$, thereby enabling us to evaluate the scalability of our methodology. The simulation's initial condition is a fully-developed flow with no forcing, so we allow the flow to develop with nonzero forcing for one period T_v before including it in the dataset. Each trajectory, which now covers $t \in [0.33, 2]$ ($5 \times T_v$), is then further partitioned into two trajectories covering $t \in [0.33, 1]$ and $t \in [1, 1.67]$ respectively. Each of these is then included in the dataset as a separate trajectory covering $2 \times T_v$ with varying initial conditions. The time domain for each trajectory is 133 time steps.

As discussed in Section 3, the forcing f corresponds to jets on the top and bottom of the cylinder which we parametrize as a zero-mean Gaussian process with covariance function $k(t_1, t_2) = \alpha \exp(-(t_1 - t_2)^2/(2\ell^2))$, where $\ell = T_v$ and $\alpha = 10^{-5}$; this setting ensures that the flow rates are mostly within the interval $[-0.01, 0.01]$. We generate 60 training, 5 validation, and 5 test trajectories for different realizations of f sampled from $\mathcal{GP}(0, k)$. These are then partitioned as described above into 120 training, 10 validation, and 10 test trajectories. Representative samples of forcing are shown in Figure 10, and a sample trajectory from the training set is shown in Figure 11.

Because the forcing is not directly parametrized, it is not as straightforward as before to estimate the

Table 6: Fluid flow with control: hyperparameter combinations chosen for latent SINDy models to minimize validation error.

ROM dim.	POD-SINDy		AE-SINDy	
	Poly. order	Threshold	Poly. order	Threshold
$d = 7$	3	0.001	3	0.001
$d = 8$	2	0.1	2	0.1
$d = 9$	2	0.03	3	0.001

intrinsic solution manifold dimension. To approximate it, we collect the sampled forcings over $t \in [0, 2]$ and project them onto their POD basis. With 6 modes, we find we capture over 99% of the kinetic energy. With time t and 6 POD coefficients to represent forcing, we can uniquely specify any point in solution space, therefore 7 is taken to be our intrinsic solution manifold dimension, and our lower bound for the ROM dimension d .

For the latent SINDy baseline, we have two primary hyperparameters to choose: the order of the polynomial basis, and the thresholding on the coefficients. To choose these, we conduct a grid search over polynomial orders $\{1, 2, 3\}$ and thresholds $\{0.001, 0.003, 0.01, 0.03, 0.1\}$ and choose the combination that minimizes mean error ε_μ over the validation set. Hyperparameters that led to unstable models on the validation set were disqualified. The chosen hyperparameters are shown in Table 6.

Architecture and training The encoder mean is a CNN that takes u as the input with the following architecture:

$$\begin{aligned} \text{Conv}[3, 32] &\xrightarrow{\text{ReLU}} \text{Conv}[32, 64] \xrightarrow{\text{ReLU}} \text{Conv}[64, 128] \xrightarrow{\text{ReLU}} \\ \text{Conv}[128, 256] &\xrightarrow{\text{ReLU}} \text{Conv}[256, 512] \xrightarrow{\text{ReLU}} \text{Linear}[n_h, d] \end{aligned}$$

where for all convolutional layers, stride is 2, padding is 2, and kernel size is 5. Note that the first layer takes a 3-channel input since this dataset consists of two-dimensional velocity and pressure fields. The hidden dimension comes out to $n_h = 21504$ for this case. The architecture for the mean of the decoder that takes z as the input is defined in a symmetric manner using transposed convolution layers as follows:

$$\begin{aligned} \text{Linear}[d, n_h] &\xrightarrow{\text{ReLU}} \text{ConvT}[512, 256] \xrightarrow{\text{ReLU}} \text{ConvT}[256, 128] \xrightarrow{\text{ReLU}} \\ \text{ConvT}[128, 64] &\xrightarrow{\text{ReLU}} \text{ConvT}[64, 32] \xrightarrow{\text{ReLU}} \text{ConvT}[32, 3] \end{aligned}$$

As in previous cases, output padding is used to recover the state dimension D . The encoder variance and decoder variance are parametrized directly, such that they are constant with respect to u and z respectively. Also as with the Burgers' equation test case, a log-normal prior is placed on the variance of the decoder.

The drift function is a feedforward neural network that takes the latent state z , forcing $f(t)$, and time as inputs with the following architecture:

$$\text{Linear}[n_i, 128] \xrightarrow{\text{ReLU}} \text{Linear}[128, 128] \xrightarrow{\text{ReLU}} \text{Linear}[128, 128] \xrightarrow{\text{ReLU}} \text{Linear}[128, d]$$

where $n_i = d + N_f = 10$. The parameters μ do not vary from trajectory to trajectory in this case, so it is not included in the drift. The dispersion matrix is, like the variance of the encoder/decoder, parametrized directly, making it constant with respect to t and μ .

Finally, the deep kernel (see Section 2.5) applies the feedforward neural network $\varphi(t)$ to each input, which is defined as

$$\text{Linear}[1, 128] \xrightarrow{\text{ReLU}} \text{Linear}[128, 512] \xrightarrow{\text{ReLU}} \text{Linear}[512, 128] \xrightarrow{\text{ReLU}} \text{Linear}[128, 1].$$

For this model and all baseline models, we train using the Adam optimizer [62] with an initial learning rate of 10^{-3} for 200 epochs and a batch size of 64. We use an exponential decay scheduler, such that the learning rate decays by 10% every 2000 iterations.